JOURNAL OF GEOPHYSICAL RESEARCH, VOL. ???, XXXX, DOI:10.1002/,

Three-dimensional dynamics of baroclinic tides over a seamount

Vasiliy Vlasenko[1], Nataliya Stashchuk[1], and W. Alex M. Nimmo-Smith[1]

Vasiliy Vlasenko, School of Biological and Marine Sciences, Plymouth University, Plymouth, PL4 8AA, UK (vvlasenko@plymouth.ac.uk)

[1]School of Biological and Marine Sciences,
Plymouth University, Plymouth, PL4 8AA,
UK.

Abstract.

The Massachusetts Institute of Technology general circulation model is used for the analysis of baroclinic tides over Anton Dohrn Seamount (ADS), in the North Atlantic. The model output is validated against in-situ data collected during the 136-th cruise of the RRS "James Cook" in May-June 2016. The observational data set includes velocity time series recorded at two moorings as well as temperature, salinity and velocity profiles collected at 22 hydrological stations. Synthesis of observational and model data enabled the reconstruction of the details of baroclinic tidal dynamics over ADS. It was found that the baroclinic tidal waves are generated in the form of tidal beams radiating from the ADS periphery to its centre, focusing tidal energy in a surface layer over the seamount's summit. This energy focusing enhances subsurface water mixing and the local generation of internal waves. The tidal beams interacting with the seasonal pycnocline generate short-scale internal waves radiating from the ADS centre. An important ecological outcome from this study concerns the pattern of residual currents generated by tides. The rectified flows over ADS have the form of a pair of dipoles, cyclonic and anti-cyclonic eddies located at the seamount's periphery. These eddies are potentially an important factor in local larvae dispersion and their escape from ADS.

1. Introduction

The oceanic floor contains around 12000 seamounts [*Wessel et al.*, 2010] that play an important role in tidal energy conversion and the formation of local ecological communities. Seamounts act as natural obstacles for currents enhancing tidal energy dissipation and water mixing. There is evidence that seamounts form hotspots of biological activity in the oceans [*Lavelle and Mohn*, 2010; *Morato et al.*, 2010]. Analysis done by *Rogers* [1994] indicates that higher species richness detected at seamounts compared to coastal or oceanic areas can be a consequence of enhanced oceanic dynamical activity in these areas [*Henry et al.*, 2014].

The primary aims of the 136-th cruise of the RRS "James Cook" (hereafter JC136) to the North East Atlantic in May-June 2016 were (i) to find a connection between the populations of corals in the bathyal zone on different seamounts, and (ii) to find a correlation between coral diversity and oceanic processes near seamounts (tides, currents, internal waves, eddies, etc.). For these purposes the ship was equipped with a remotely operating vehicle (ROV) ISIS that conducted surveys and collected samples of biological species from the Anton Dorhn, Rockal Bank, George Bligh, and Rosemary Seamounts, as well as from the Wyville Thomson Ridge. The principal part of the oceanographic measurements included deployment of two moorings and CTD-LADCP sampling in the area of Anton Dohrn Seamount (ADS), located to the west of Scotland in the central part of the Rockall Trough. This seamount, or table-mount guyot, is a former volcano with nearly circular shape and about 40 km in diameter, Figure 1. ADS rises approximately 1800 m above the bottom with minimum depth in its centre of about 530 m.

A large number of theoretical and experimental papers have been published on dynamical processes over seamounts, e.g barotropic and baroclinic tides, generation of internal waves, mixing, response to stationary currents, formation of residual circulation, eddies, etc. An overview of the most significant publications can be found in *Vlasenko et al.* [2013]. The primary goal of the present paper is to report a new set of observational data collected during JC136 near ADS. These data were used for setting a numerical model and its further validation. An overall goal of these model efforts was to investigate the tidal regime around ADS that took place during the JC136 cruise. The comprehensive model output allowed us to build up a complete picture of possible motions developing in the area, specifically, baroclinic tidal energy focusing over the bank, local generation of internal waves due to interaction of tidal beams with the seasonal pycnocline, and the generation of residual currents and their possible implication for larvae dispersion.

The paper is organised as follows. The measurement techniques and collected data are presented in Section 2, along with the model set-up. The next section reports the effect of the focusing of baroclinic tidal energy over the ADS summit. The mechanism of local generation of internal waves is discussed in Section 4. Tidally generated residual currents and their possible implications for larvae dispersion are analysed in Section 5. Finally, Section 6 summarises all principal findings.

2. Measurements and model set up

2.1. Observational data set

Figure 1 shows the scheme of the field experiment conducted on JC136 cruise. The observational campaign included 18 CTD stations, deployment of two moorings, M1 and M2, and four dives of the ROV ISIS. Note that CTD stations 4-19 located at the edge of

steep topography were repeated at the same site (yo-yo) on 19th May 2016 when ROV dives were suspended due to bad weather conditions. At the end of the cruise (on 17th June 2016) three CTD stations, 41-43, were conducted along the cross-bank transect shown in Figure 1. A Lowered Acoustic Doppler Current Profiler (LADCP) was mounted at the CTD rosette, so vertical profiles of horizontal velocities were recorded at each station. The obtained data were processed with the LDEO LADCP Processing Software developed by *Visbeck* [2002].

Moorings M1 and M2 were equipped with an upward-looking 75 kHz Acoustic Doppler Current Profilers (ADCP) and a 600 KHz downward-looking ADCP for measuring the flow regime in the bottom boundary layer. Details of moorings instruments are provided in Table 1. Table 2 shows the coordinates of ROV dives 270, 271, 272, and 292 that were used for modelling larvae dispersion. The collected data set was complemented with a velocity time series recorded by a vessel mounted ADCP (150kHz) during ROV dive 296.

2.2. The model

The fully nonlinear nonhydrostatic Massachusetts Institute of Technology general circulation model (MITgcm, *Marshall et al.* [1997]) was used for modelling the wave dynamics near ADS. The semi-diurnal M_2 tidal harmonics predominates in the area [*Egbert and Erofeeva*, 2002], so we restricted our analysis by considering only this tidal constituent. The tidal forcing was activated in the model using an external software package added to the MITgcm code that sets a tidal potential in the RHS of the momentum balance equations. Two tidal components were introduced as follows [*Stashchuk et al.*, 2017]

$$U = A\sin(\omega t + \phi), \quad V = B\sin(\omega t), \tag{1}$$

where U and V are zonal and meridional water discharge, respectively, ω is the tidal frequency, and ϕ is the phase lag that controls the tidal ellipse inclination. The main part of the field campaign was conducted during the transition from neap to spring tide, so for setting the tide in the model we used A=50 m^2 s^{-1}, B=100 m^2 s^{-1}, and $\phi = \pi/4.1$, which provides a good coincidence with the ellipses of the inverse tidal model TPXO8.1 [*Egbert and Erofeeva*, 2002], Figure 2 a. A non-slip boundary condition was used at the bottom.

The model domain included 768×794 grid points. Its central part with 512×538 grid points and horizontal resolution $\Delta x = \Delta y$=115 m was used for the analysis. The lateral grid areas that included 118 grid points were added at each side of the model domain. Here the grid step was increased telescopically from 115 m in the central part to 5500 m towards the boundaries. Such a grid stretching allows one to radiate internal waves from the central area without their backward reflection from the boundaries. Another 10 boundary steps of the model domain at the periphery were added to release the barotropic tidal waves from the area. Here the grid step increased to $2{\cdot}10^8$ m at the model boundary. Such a combination of a two-step telescopic grids eliminates reflection of both barotropic and internal waves from the outer boundaries during the ten days of the numerical experiment.

The vertical grid step was Δz =10 m which provided quite a detailed resolution of tidally induced baroclinic fields. The fluid stratification was taken from CTD data recorded at station 1. The buoyancy frequency profile (blue line) is shown in Figure 2 b together with the smoothed profile (the red line).

The coefficients of horizontal viscosity were taken at the level of 10^{-2} m^2 s^{-1}. The vertical turbulent closure for the coefficients of vertical viscosity ν and diffusivity κ was provided by the Richardson number dependent parametrisation, [*Pacanowski and Philan-*

107 *der*, 1981]:

$$\nu = \frac{\nu_0}{(1+\mu \mathrm{Ri})^n} + \nu_b,$$
$$\kappa = \frac{\nu}{(1+\mu \mathrm{Ri})} + \kappa_b. \quad (2)$$

109 Here Ri is the Richardson number, $\mathrm{Ri} = N^2(z)/(u_z^2 + v_z^2)$, and $N^2(z) = -(g/\rho)(\partial\rho/\partial z)$
110 is the buoyancy frequency (g is the acceleration due to gravity, and ρ is the density),
111 u and v are zonal and meridional velocities; ν_b=$10^{-5}\,\mathrm{m^2\,s^{-1}}$ and κ_b=$10^{-5}\ \mathrm{m^2\,s^{-1}}$ are the
112 background parameters, ν_0=$1.5{\cdot}10^{-2}\,\mathrm{m^2\ s^{-1}}$, μ=5 and n=1 are the adjustable parameters.
113 Such a parametrisation increases coefficients ν and κ in the areas where the Richardson
114 number is small to take into account the mixing processes induced by shear instabilities
115 and breaking internal waves. A systematic analysis of the sensitivity of the model output
116 to the parameters ν_b, κ_b, ν_0, μ, and n was conducted in [*Stashchuk and Hutter*, 2001].
117 It was found that with the above mentioned parameters formula (2) keeps the diffusivity
118 and viscosity at the level sufficient for the model stability. On the other hand, this level
119 of mixing and viscosity does not affect substantially the internal wave fields.

3. Tidal beams and energy focusing

120 We start our analysis with consideration of the velocity profiles recorded at CTD stations
121 41-43, Figure 1. The vertical profiles of instantaneous horizontal velocity $\sqrt{u^2+v^2}$ are
122 shown in Figures 3 a, 3 b, and 3 c by thick lines. These profiles clearly show evidence of
123 local velocity maxima located at different depths at stations 41-43. Specifically, Figure 3 a,
124 shows intensification of the surface currents at 100 m depth at station 43, just over the top
125 of ADS. The deepest maximum was recorded at 750 m depth at station 41 conducted at
126 the bank edge, Figure 3 c. In between, at station 42, the maximum of horizontal velocity
127 was found in the intermediate layer at 330 m depth, Figure 3 b.

A series of model-based sampling was arranged in a similar way to the observations, i.e. at the positions of CTD stations 41-43. Twelve vertical profiles of $\sqrt{u^2+v^2}$ spanning the CTD sampling time (an approximate duration of CTD samplings in the cruise was one hour) with 5-min time interval are shown in Figures 3 a, 3 b, and 3 c by thin light lines. Comparison of $\sqrt{u^2+v^2}$ profiles reveals that the positions of the extrema of the observed and model predicted profiles coincide. The level of theoretical and experimental amplitude velocities in these layers is also in a good agreement except probably the surface 200 m layer at station 43. The 50-100% inconsistency between theoretical and experimental profiles visible in the surface layer in Figures 3 a could be a consequence of a surface current that existed in the area during the field experiment, but which was not set in the model because of the lack of the observational data for its validation. Another reason for the reported inconsistency could be imperfection of the LADCP processing procedure [*Visbeck*, 2002] which underestimates currents near sea surface. This issue was discussed by *Aleinik et al.* [2007] who showed that the error in the velocity in the surface layer can be as large as 0.06-0.08 $\mathrm{m\,s^{-1}}$. Thus, taking into account this reasoning one can conclude that the model reproduces the wave dynamics in the ADS area correctly.

The reason for the reported velocity maxima at different depths can be explained by considering the spatial distribution of the amplitude of the horizontal velocities $\sqrt{u^2+v^2}$ over one tidal cycle which is shown in Figure 3 d for the transect a-a (see Figure 1). This figure reveals evidence of two tidal beams generated at the sharp edges of the bank topography (at points A and B). They propagate upward and meet at the centre of the bank in the subsurface 200 m layer. The tidal-beam (or T-beam) interpretation of Figure

3 d is confirmed by the positions of the curves

$$\int \frac{dz}{\alpha(z)} = \pm x + \text{const}, \quad \alpha(z) = \sqrt{\frac{\omega^2 - f^2}{N^2(z) - \omega^2}}, \tag{3}$$

shown in Figure 3 d by dashed lines. In this equation x and z are horizontal and vertical coordinates, f is the Coriolis parameter, and $N(z)$ is the buoyancy frequency. In fact, dashed contours in Figure 3 d are the characteristic lines of the wave equation

$$w_{xx} - \alpha^2(z) w_{zz} = 0, \tag{4}$$

where w is the vertical wave velocity. Coincidence of these lines with zones of velocity maxima confirms a T-beam origin of the latter.

ADS is a circular guyot, Figure 1. One can assume that the T-beam mechanism of generation of internal waves works also in all other cross-sections around ADS (a similar case was considered by *Baines* [2007] for a symmetrical cylindrical seamount). As a result of the seamount symmetry, the tidal energy propagating from many sites at the bank periphery to its centre focuses over the top of ADS where station 43 was located. From theoretical predictions a large area of high concentration of tidal energy should be expected just over the seamount summit, which is obviously evident in Figure 3 d in the surface 200 m layer.

Additional observational evidence of the T-beam generation can be found in the mooring time series. According to Figure 3 d, both moorings, M1 and M2, were deployed in the area where the T-beam could be recorded as a strong amplification of horizontal velocities at depths around 800 m. In other words, the tidal beam should be seen in the moorings velocity time series, as well. Figures 4 a and 4 c clearly show intensification of zonal and meridional velocities in the bottom layer, specifically, below 700 m depth for mooring M1.

The model time series were recorded with a 20 s time interval at the position of mooring M1. They are presented in Figures 4 b (zonal velocity) and 4 d (meridional velocity). Comparison of the left and right patterns in Figure 4 shows their consistency.

Similar time series recorded at mooring M2 and reproduced numerically for the same time span are shown in Figure 5. The model predicts that the position of the tidal beam at this mooring should be at depths between 800 m and 1000 m, Figure 3 d. Figure 5 demonstrates intensification of the tidal velocity in this layer, both in observational and model time series. The only difference between moorings M1 and M2 is that the latter was deployed deeper than M1, i.e. at the 1200 m isobath. According to the tidal beam position shown in Figure 3 d, no substantial currents at mooring M2 below 1000 m depth are expected. This is exactly what Figure 5 demonstrates, both in observations and in the model predictions.

Analysis of the mooring data can be complemented by considering vertical oscillations. Figure 6 presents vertical velocities recorded at both moorings, M1 and M2, and predicted by the model. This figure reveals tidal periodicity which is clearly visible in the mooring M2 time series (panel c). This strong tidal signal recorded in the 700-1000 m layer is associated with the tidal beam discussed above. In addition to that, one can identify also a large number of positive and negative short-term pulses. They are present both in observational and model time series and cover a large part of the water column. Joint analysis of vertical velocities with model predicted temperature time series presented in Figures 6 b and 6 d by black solid lines (isotherms are shown with 0.2° interval) reveals a strong correlation of short-term pulses evident in velocity records with vertical displace-

ments of isotherms in the seasonal thermocline produced by short period internal waves. The latter appear in packets with tidal periodicity indicating their tidal origin.

Two classes of internal waves visible in Figures 6 b and 6 d, i.e. short period packets and long term semi-diurnal waves, are separated in space occupying different parts of the water column. Short-period internal waves are mostly seen in the surface layer (that coincides with the seasonal thermocline), whereas long-period semidiurnal oscillations (classified above as evidence of the tidal beam) exist mostly below 600 m depth with largest amplitude at the depths of the main pycnocline, Figure 2.

Two different classes of internal waves generated in the ADS area are visible also in Figures 7 and 8. Figure 7 a represents a time series of the temperature profiles recorded on 19-th of May 2016 as repeated casts (yo-yo) with roughly 40 min time interval between samplings, and Figure 7 c shows this data as a set of vertical profiles. Figures 7 b and 7 d show similar time series and the yo-yo temperature profiles produced by the model. One of the conclusions that can be drawn from the comparison of the in-situ collected data and the model output is their similarity which testifies an ability of the model to reproduce wave dynamics in the ADS area. This remark concerns consistency of the temperature records above 600 m depth, both in experimental and theoretical profiles, and their variability below 700 m depth.

Such a diversity of the temperature profiles below 600-metre depth can be explained in terms of vertical oscillations developed in the layer occupied by the tidal beam. Simple estimations based on Figure 7 a show that vertical displacements of isotherms from their stationary position can exceed 100 m. Bearing in mind that the yo-yo station was conducted at the periphery of ADS where the tidal beam is located below 600 m, one can

conclude that recorded variability of the temperature profiles in this layer (visible also in Figure 3) can be treated as evidence of the tidal beam discussed above.

Quite a different wave dynamics were observed in the surface layer. Figures 6 b and 6 d show packets of short-period internal waves in the sub-surface layer predicted by the model. In the field experiment both ADCPs were unable to capture signals from the sub-surface layer (see Figures 4 a, 4 c; 5 a, 5 c; 6 a, 6 c). However, the ship-mounted ADCP was active during ROV missions, and the time series of the meridional and zonal velocities recorded during dive 296 are shown in Figures 8 a and b. Similar model predicted time series for the positions of moorings M1 and M2 are presented in Figures 8 c-f providing evidence of short period internal wave packets in the upper 250 m. The numerical model predicts their propagation northward, i.e. from mooring M1 to mooring M2. The velocity time series recorded by the ship mounted ADCP also confirms their northward propagation in the area of moorings M1 and M2, see Figure 1. Bearing in mind that the bottom topography over the ADS summit is quite flat (Figures 1-3) and the total depth there is about 600 m, it is quite unlikely that the recorded short period internal waves were generated over the top of the seamount according to a standard mechanism of tide-topography interaction. Clarification of the conditions for their generation is an objective of the next section.

4. Mechanisms of generation of internal waves

4.1. Local generation of internal waves

A relatively simple way to identify the potential locations of internal tide generation is to follow the methodology suggested by *Baines* [1982] localising the positions of the

maxima of the internal body force (IBF). In a two-dimensional (x, z) case the IBF is:

$$\mathrm{IBF} = \rho_0 u_{\mathrm{tide}} H(x) z \frac{N^2(z)}{\omega} \left[\frac{1}{H(x)}\right]_x . \quad (5)$$

Here u_{tide} is the amplitude of the barotropic tidal current; $H(x)$ is the bottom profile; ρ_0 is the mean density. In our case, the spatial distribution of the IBF in the meridional across-bank section is presented in Figure 9 a.

It is clear from the IBF normalized distribution that the maximum of tidal energy conversion (generation of internal tides) should take place over the seamount's flanks, specifically, in the areas with centres 57.23^{o}N at the south and 57.62^{o}N at the north of ADS. Note that the latitude 57.62^{o}N is located just between moorings M1 and M2. Thus, assuming the generation of the short period wave packets recorded during the ROV's dive 296 (shown in Figure 8), specifically in the area of the IBF maximum, these packets should propagate in opposite directions at moorings M1 and M2. However, according to Figures 8 b and 8 d, they propagate in the same direction, i.e. northward. Taking into account a one-hour time lag between arrival of the waves at moorings M1 and M2, Figures 8 b and 8 d, these waves should propagate from somewhere near the bank summit. Based solely on the distance between the moorings and the recorded time lag one can estimate the horizontal phase speed of the packet as c=0.74 m s^{-1} which looks quite realistic for the considered area (see also estimates below).

4.2. Lee wave mechanism

Another possible scenario for short-period waves generation could be a lee-wave mechanism, which usually takes place near abrupt changes of bottom topography. Specifically, internal lee waves are generated downstream of the bottom topography by a strong su-

percritical tidal flow. They are released and propagate upstream when tidal flow slackens. The feasibility of lee wave generation appears when the Froude number, $\mathrm{Fr} = u_{\mathrm{tide}}/c$, is equal to or larger than 1. The phase speed c of internal lee waves is calculated from the boundary value problem (BVP) for short-scale internal waves [*Vlasenko et al.*, 2005]

$$\Phi_{zz} + \frac{N^2(z)}{c^2}\Phi = 0, \quad \Phi(-H) = \Phi(0) = 0.$$

Here the eigen function Φ is the vertical structure function of internal waves. The estimation of Fr for the ADS area has shown that its maximum value hardly exceeds 0.4, which is insufficient for the lee wave mechanism to be realistic. It is interesting that the value of the phase speed for the first baroclinic mode in the area of M1 and M2 varies between $0.6\,\mathrm{m\,s^{-1}}$ and $0.9\,\mathrm{m\,s^{-1}}$, which is close to the phase speed of the wave packet calculated in previous subsection.

4.3. T-beam generation mechanism

The above analysis has shown that neither IBF theory, nor the lee-wave mechanism can explain the origin of the short-period internal waves propagating from the seamount centre. Another hypothesis to be tested is the "local" generation of internal waves due to the interaction of tidal beams with the seasonal pycnocline (hereafter, the T-beam generation mechanism). The possibility of such a scenario can be concluded from the analysis of Figure 3 where two tidal beam systems generated over ADS are clearly seen. In space these beams follow the characteristic lines (3) of the wave equation (4). Figure 9 a shows two families of characteristic lines (lines AD and BC) for the transect along 11.1°W latitude that crosses the ADS centre. The characteristic lines touch the bottom at points A and B where their inclination coincides with the bottom steepness and where the tidal

beams are generated (see also Figure 3 d). As discussed above, the tidal beams propagating upward from the ADS periphery meet in the subsurface layer over the seamount's top (in the area between points C and D) where they hit the seasonal pycnocline. The latter starts to oscillate vertically with tidal frequency producing a series of progressive internal waves radiating from the centre of generation [*Gerkema*, 2001].

The process of local T-beam generation can be demonstrated using the Hovmöller diagram, Figure 9 b. Here the model predicted evolution of the 12°C (equilibrium depth 31 m) isotherm along the 11.1°W transect is presented at one hour intervals with time increasing from the top to the bottom. The ADS profile is shown here at the bottom of the figure. To visualise the wave evolution, the leading waves in each packet are connected by straight red lines. The wave trajectories clearly show that internal waves originate in the middle of ADS, specifically in the area of the C-D section, confirming the idea of local T-beam generation of internal waves due to interaction of tidal beams with the pycnocline. As was shown in *Vlasenko and Stashchuk* [2006, 2015], due to changing hydrological conditions and radial divergence, waves propagating seaward weaken in amplitude and can transform into different wave forms including high baroclinic modes [*Vlasenko*, 1994].

Note that the two-dimensional interpretation of local generation given above is not always applicable [*Vlasenko et al.*, 2014]. It can be extended to many other transects across the bank making the presentation substantially three-dimensional. For the three-dimensional analysis we use the amplitude of $\sqrt{u^2+v^2}$ at the free surface, Figure 10 a. Its spatial distribution shows the location of the T-beam generation and the main routes of the propagating waves. In Figure 10 a the wave fronts can be traced as the areas with the largest velocity values. They are seen as red arcs that radiate from the areas around

the seamount summit marked by letters C and D. The latter coincide with the positions of C and D shown in Figures 9 a and 9 b.

The intensity of the velocity amplitudes of the generated waves is not evenly distributed in space. It predominates mostly in the direction of the orientation of the major semi-axis of tidal ellipses shown in Figure 10 a. This predominance of north-east and south-west orientation of internal wave radiation can be explained also in terms of tidal energy conversion discussed above, specifically, considering the positions of the generation of tidal beams with respect to the topography. Figure 10 b shows amplitudes of horizontal velocity $\sqrt{u^2+v^2}$ 10 m above the bottom. The position of points A and B in this graph is the same as that shown in Figure 9 a. As one can see, these areas are the most energetic in terms of tidal activity. In conjunction with Figures 3 d, 9 a, 10 a one can conclude that focusing of baroclinic tidal energy over ADS summit triggers the mechanism of local T-beam generation of internal waves in the area.

Another confirmation of local generation of internal waves over the ADS summit due to the T-beam mechanism was found in a series of numerical experiments with an idealised seamount

$$H(x,y) = 1500 - 3000\exp\{-[(x-x_s)^2 + (y-y_s)^2]/2500\}$$

where x_s and y_s are the coordinates of its centre. The seamount's height, $H(x,z)$, was cut off at 700 m depth (minimum depth over ADS), and the sharp edges were smoothed by moving average across the topography from the seamount centre to its periphery using ten neighbouring grid points (Figure 11). The tidal parameters in these experiments were $A = B$=100 $\mathrm{m^2\,s^{-1}}$, and $\phi = \pi/2$ which turn the tidal ellipse (1) into a perfect circle.

The upper panel of Figure 11 shows the sea surface displacements produced by internal waves over this symmetrical table seamount after 57 hours of model time. Analysis of the wave fronts' structure and their spatial evolution reveals that the strongest waves are generated within the red dotted circle, i.e. in a region above the flat bottom from which they propagate radially decreasing in amplitude as spiral-type waves. Thus Figure 11 confirms that the only possible explanation for these waves generation is the T-beam mechanism.

Maximum isotherm displacements in the epicentre of the generation area reach 20 m (see also Figure 6 b), which is several times smaller than the internal tidal oscillations in the tidal beams (∼100 m). Parameters of the short-scale internal waves generated by tidal beams over idealized seamount or in the centre of ADS (these waves are visible in Figures 6, 8, 9, 11) can be sensitive to the level of the background mixing and the model resolution. Analysis of the sensitivity of the model output to the coefficient of the horizontal diffusion and grid step is presented in Appendix B.

4.4. Implication for water mixing

It is expected that tidally generated internal waves can modify the background stratification by inducing mixing. Zones with strong mixing can be identified using the Richardson number Ri. According to *Miles* [1961] and *Howard* [1961], some level of mixing (turbulence) is expected in regions where the Richardson number Ri drops below 1/4 at least for a short period of time. *Abarbanel et al.* [1984] showed later that flows can be unstable even with $\mathrm{Ri} > 1/4$, so for the qualitative analysis below we will take $\mathrm{Ri} = 1$ as a threshold for possible mixing events.

Figure 12 a shows the area of the minimal Richardson numbers over one tidal cycle along the transect a-a, Figure 1, where Ri drops below 1. This pattern is overlaid with the amplitudes of horizontal velocities $\sqrt{u^2+v^2}$ to depict the positions of the tidal beams. The $0.2\,\mathrm{m\,s^{-1}}$ isoline is shown by a solid black line. The smallest values of the Richardson number are seen in the place where two tidal beams intersect between 50 m and 400 m depths just in the centre over the seamount summit. According to Figure 2 b, the buoyancy frequency here drops to $0.0013\,\mathrm{s^{-1}}$, so strong vertical velocity shears associated with tidal beams can reduce the Richardson number in this layer below the critical level.

An obvious indicator for mixing processes can be the difference ΔT between the initial background temperature T_0 and the temperature $< T >$ modified by the wave mixing

$$\Delta T =< T > -T_0.$$

Here $< T >$ is the temperature field averaged over one tidal period. Figure 12 b presents the temperature difference ΔT produced by internal wave mixing along section a-a (Figure 1) over five tidal periods. It shows a considerable drop of the temperature (up to 0.3°) in the surface layer and a similar temperature rise just below this layer. This temperature evolution can be treated in terms of internal wave activity that intensifies vertical mixing in the seasonal pycnocline. As it was shown in Figure 10 a, the areas of enhanced internal wave mixing are not evenly distributed in space. The temperature change ΔT at the depth of 30 m occupies a larger area to the south-south-west of the ADS summit than anywhere else, Figure 12 c. This happens because of the strongest T-beam generation of internal waves in this area.

As observational evidence of the intensification of local water mixing over the top of ADS due to internal waves, the temperature profile recorded at CTD station 43, which

was inside a simulated region of cooling shown in Figure 12 c, reveals substantially lower temperature in the surface layer in comparison with those measured at CTD stations 41 and 42 (Figure 12 d). This result is in agreement with the satellite observations (NASA Giovanni Web Portal https://giovanni.gsfc.nasa.gov/giovanni/) of the sea surface temperature (SST) collected by the MODIS-Aqua satellite. The SST anomalies calculated as a deviation from a long-term (years 2003-2016) mean May-August SST are shown in Figure 13. Large-scale zonal and meridional gradients have been subtracted from the SST field using a two-dimensional third-order polynomial. A very large area with SST more than 0.1°C lower than the surrounding area is located just over ADS (Figure 13). This feature resulting from enhanced vertical mixing can be treated in terms of the mechanism of baroclinic tidal energy focussing discussed above.

5. Residual tidal currents

In addition to internal waves, residual currents are also generated by periodical tidal flow over variable topography. These currents can be quite strong exceeding $10\,\mathrm{cm\,s^{-1}}$ over the Malin Sea slope/shelf [*Stashchuk et al.*, 2017] or even more than $20\,\mathrm{cm\,s^{-1}}$, around the area of Georges Bank [*Loder*, 1980].

As distinct from shelf/slope areas where residual tidal currents normally take the form of along-slope flows [*Huthnance*, 1973] in three dimensions a periodically alternating tidal flow interacting with a seamount generates a dipole of eddies and density anomalies rotating around the seamount [*Haidvogel et al.*, 1993]. Note, however, that the tidal forcing in the latter model was activated by a periodic barotropic discharge prescribed at one open boundary, whereas three other boundaries were taken as rigid walls. Such an approach results in the generation of standing waves instead of progressive waves and inertial os-

cillations that do not reproduce real tidal flow over an isolated bank located in the open sea.

To determine the structure of the residual currents over ADS, we configured the model for an idealised Gaussian bank and calculated the residual tidal fields both for homogeneous and stratified fluids. The results are presented in the Appendix. As is shown there, an oscillating tidal flow generates two pairs of quasi-stationary cyclonic and anticyclonic eddies. A similar structure of residual currents over a Gaussian-type underwater bank was also reported by *Pingree and Maddock* [1980], who modelled a system of vertically integrated equations with quadratic terms for vertical viscosity. The intensity of these eddies is sensitive to the parameters of the tidal ellipses, specifically, to the length of the minor axis. The numerical experiments with the Gaussian seamount have shown that the smaller the minor axis, the stronger the residual currents. Water stratification also introduces some important effects changing the position of the eddies (for details see the Appendix).

These results obtained for an idealised bank are quite useful for interpretation of the spatial structure and evolution of the residual currents generated over real three-dimensional topographies. Figure 14 a shows the structure of the residual currents in the ADS area which resembled the picture of two eddy dipoles generated over an idealised seamount, Figure A.2 b, in particular. Of course, the imperfect asymmetric shape of the ADS topography results in violation of the symmetry of this pattern.

The transect of the residual zonal and meridional velocities along the Ellett Line (a regular annual CTD section across the Rockall Trough that includes ADS that has been sustained since 1975, www.o-snap.org) are shown in Figures 14 b and 14 c. The spatial

413 structure of these model-predicted residual currents and their intensity are consistent with
414 that recorded in-situ in mid-June 2009, [*Sherwin et al.*, 2015]. Figure 14 shows that in
415 the vertical direction the eddies extend from the surface to the bottom of the seamount
416 having mostly constant velocity over the whole water column.

5.1. Biological implications

417 Recent investigations by *Henry et al.* [2014] around Hebrides Terrace Seamount (North-
418 East Atlantic ocean) have suggested that internal tides may enhance biological diversity
419 on this and adjacent seamounts in the Rockall Trough. As shown above, oceanic tides
420 generate internal waves, residual currents, and eddies around ADS, which can facilitate
421 larvae dispersion between adjacent seamounts.

422 An underwater survey of ADS conducted using the ROV revealed a wide variety of
423 biological species (sponges, corals, etc) in different parts at the ADS summit. It is clear
424 that dynamical processes developing in the area can have strong effect on larvae dispersion.
425 To understand possible larvae trajectories we used a passive tracer approach assuming that
426 the larvae can be considered as floating particles transported by currents. To predict the
427 positions of particles at some designated moments of time we used a Lagrangian approach
428 with a method of multivariate interpolation on a 3-dimensional regular grid based on 5-
429 minute model outputs of the three velocity components. The prediction time chosen for
430 these experiments was 40 days which equals the time span required for larvae of marine
431 corals to complete their life cycle [*Larsson et al.*, 2014]. (Nematocysts appear when larvae
432 are 30 days old and if nematocysts are used for primary anchoring, this could indicate
433 that larvae are capable to settle at this time. The larvae survived for a maximum 57 days
434 in the laboratory.)

A large number of experiments revealed several realistic scenarios of larvae dispersion. In general, the vast majority of particles moved around the bank transported by residual currents. They were deposited at different places giving birth to new local colonies of corals. Some particles escape from the bank and can be considered as a potential source for wider spreading in the marine environment. We illustrate here the most interesting trajectories of four particular experiments. The particles started their journey from four different positions where the ROV conducted its dives, Figure 1. Specifically, one particle started from the seamount summit (dive 272), and three others from the northern flank of ADS (dives 270, 271, and 296). Geographically their positions were very close to each other, although due to steep topography they started at very different depths, i.e. at 800 m, 1000 m, and 1100 m.

Figure 15 a shows a plan view of the trajectories of the particles overlapped with the field of residual currents, and Figure 15 b represents the particle tracks in three dimensions. The complex structure of the residual currents around the bank has a clear effect on the particle dispersion. Particles marked by green and red (dives 296 and 270) moved clockwise and the particle coloured with blue (dive 271) propagated counter-clockwise. Two particles in the north-east part left the seamount with strong outgoing currents. Another couple of particles do the same but at the south-western part of seamount. Figure 15 b shows that trajectories of particles are quite complicated in three dimensions. They show the potential for larvae to change depth with ascending or descending currents generated around the seamount, which is quite important for their wider dispersion.

6. Conclusions

The most significant results from the present study on investigation of tidal dynamics around Anton Dohrn Seamount can be split into three categories:

- **Baroclinic tidal energy focusing over the seamount's summit**

The ADS flanks are supercritical in terms of baroclinic tide generation (Figures 3 d and 9 a). These are the necessary conditions for baroclinic tidal beam generation [*Vlasenko et al.*, 2005]. These beams propagate from the bank periphery to its centre focusing tidal energy over the top, similar to the mechanism of tidal energy focusing in canyons [*Vlasenko et al.*, 2016]. This mechanism resembles the effect of focusing in optical lenses. As a result, a large area of high internal tidal energy is created just over the seamount summit. This energy focusing, Figures 3 d, can have a great implication on water mixing over the top of seamounts and local generation of internal waves (T-beam generation).

- **Local T-beam generation**

The local generation of internal waves by tidal beams focusing in the ADS centre and their interaction with the seasonal pycnocline is confirmed in this study. Long ago this effect, called "local generation", was discovered by *Pingree and Mardell* [1981, 1985] who were probably the first who observed this effect in-situ. The physical explanation of this process was given by *Gerkema* [2001]. The novel element of our study is that local T-beam generation is confirmed for a circular bank, specifically, over its centre where tidal beams intersect as a result of energy focusing. Taking into account that there are more than 12000 seamounts in World's Oceans [*Wessel et al.*, 2010] the conclusions of the present study may be relevant to many other sites around the world.

477 • **Residual currents, eddies**

478 The most interesting ecological outcome from this study concerns the pattern of the
479 residual currents generated by tides interacting with an isolated seamount. This effect
480 resulting from tidal rectification along 2-dimensional topography was explained by *Huth-*
481 *nance* [1973] and *Loder* [1980]. In application to a 3D object like ADS this theory predicts
482 generation of two dipoles of cyclonic and anti-cyclonic eddies located at the seamount's
483 periphery, *Stashchuk et al.* [2017]. They can be an important factor in coral larvae disper-
484 sion including their escape from the seamount and travel to other banks of the World's
485 Ocean.

Appendix A: Residual tidal currents over an idealized Gaussian bank

The theory of tidally induced residual flows over an inclined bottom was developed by *Huthnance* [1973] and modified by *Loder* [1980] who compared the theoretically predicted slope currents with numerical outputs for the area of Georges Bank. More recent numerical experiments conducted by *Flexas et al.* [2015] have shown that the effect of tidally generated residual slope currents can be one of the major driving forces for water circulation in the Weddell-Scotia confluence, the principal area for formation of the global meridional overturning circulation. The effect of tidally induced residual currents was reviewed by *Stashchuk et al.* [2017] who conducted a systematic comparison analysis of the model predicted slope currents with a theoretical formulae developed similar to *Huthnance* [1973] and *Loder* [1980]. Consistency of numerical and analytical solutions testifies to the fact that the effect of tidally induced residual currents is quite remarkable and should be taken into account in the analysis of water circulation in many areas. Below we provide an analysis of the residual flows generated over an idealized Gaussian bank. These experiments can shed light on the dynamics we can expect in the ADS area. The shape of the bank for these experiments was taken as follows:

$$H(x,y) = 1000 - 400\exp\{-[(x-x_s)^2 + (y-y_s)^2]/800\}, \tag{A1}$$

where $H(x,y)$ is the bottom profile and x_s and y_s are the coordinates of the seamount's centre. The tidal currents were set in the model according to (1) with $A = B$=100 $\mathrm{m^2\,s^{-1}}$ (close to the discharge considered in the main series of runs). The configuration of tidal ellipses was set by the phase ϕ: ϕ=0 corresponds to a periodical reversal flow, whereas $\phi = \pi/2$ defines a perfect circle. The tidal phase ϕ between 0 and $\pi/2$ sets a tidal ellipse.

A1. Barotropic response

In homogeneous fluids the tidally induced along-slope residual current v^c over a meridionally oriented continental slope can be calculated using the following formula [*Stashchuk et al.*, 2017]:

$$v^c = \frac{AB\cos(\phi)}{2C_D\sqrt{A^2+B^2}}\frac{1}{H(x)}\frac{\partial H(x)}{\partial x}. \tag{A2}$$

Here $H(x)$ is the bottom profile across the slope, and $C_d = 0.013$. Applying this formulae to a singular circular object like the Gaussian seamount defined by (A1), one should take into account the orientation of the bottom gradient as well. An accurate correction of (A2) that takes into account the bottom orientation and the coordinate transforms was provided in *Stashchuk et al.* [2017]. Considering positions at the periphery of the bank and moving around it along isobaths this formulae predicts that the residual along-bank slope current should change its sign four times depending on the location of the quadrant where it is applied. As a result of this spatial variability, four eddies are expected to be generated over the bank according to this analysis. This is exactly what the MITgcm predicts for the Gaussian-type bank (A1).

Figure A.1 shows patterns of residual currents (middle row) and the vorticity $u_y - v_x$ (bottom row) at a depth of 600 m for three different tidal configurations. A reversal tidal flow mostly typical for weak rotation is presented in the left column ($\phi = 0$), the mid-latitude conditions are reproduced in the middle column ($\phi = \pi/4$), and the case of strong rotation is shown in the right column ($\phi = \pi/2$). It is clear from Figure A.1 that the MITgcm predicts the generation of four eddies over the seamount top: two cyclonic eddies arranged along the major tidal semi-axis, and two anti-cyclonic eddies whose positions are

consistent with the direction of the minor semi-axis. The vorticity patterns also clearly show the location of two pairs of cyclonic and anti-cyclonic eddies.

It is interesting that formulae (A2) predicts zero residual currents for the case of a complete symmetry with $\phi = \pi/2$. This conclusion is consistent with the MITgcm output that does not predict significant residual currents for an axisymmetric case (right column).

A2. Baroclinic efects

Stratification introduces quite a drastic reconfiguration of the structure of the residual flows. Figure A.2 shows a spatial distribution of the residual currents over the Gaussian bank overlaid with vertical velocities at a depth of 600 m obtained for homogeneous (Figure A.2 a) and stratified (Figure A.2 b) fluids. The stratification is that shown in Figure 2 b. For this experiment the same tidal parameters as above were taken, i.e. $A = B$=100 $\mathrm{m^2\,s^{-1}}$ and $\phi = 0$.

Comparison of Figures A.2 a and A.2 b shows that they are quite different. The baroclinic residual currents suppress the barotropic signal and reconfigure the entire spatial structure. First of all, the strongest currents are oriented now in the direction of the major axis of the tidal ellipse. In fact, this is the direction of propagation of the strongest internal waves generated over the bank and radiated from it. The position of the four eddies has also been changed. They were turned counter-clockwise by the angle of $\pi/4$ to be consistent with the direction of internal wave propagation.

An even more drastic change has been introduced to the vertical velocity field. It does not resemble the barotropic case at all; the velocity patterns in both cases are completely different. First of all, the baroclinic vertical velocity currents are ten times stronger. Secondly, the strongest downwelling area is located just over the top of the bank, not at

its the periphery as in the barotropic case. And finally, the positive upward water fluxes are located on either sides of the downwelling area. Overall, the baroclinic residual tidal signal looks much stronger.

Appendix B: Sensitivity to background mixing and grid resolution

Relatively high horizontal diffusion can reduce wave amplitudes. In the model the horizontal diffusion is introduced both explicitly by setting the coefficient of the horizontal diffusion as an input parameter (equal to 0.01 m^2s^{-1} in our case) and implicitly by setting the horizontal resolution which defines the numerical diffusion. The latter is always difficult for estimation based solely on the model output. However, in some cases it can be calculated accurately comparing an analytical solution of the diffusion equation and the model output from dye release experiments [*Stashchuk et al.*, 2014].

In order to investigate sensitivity of the model output to the diffusion coefficient and horizontal resolution in our case a series of extra numerical experiments was conducted with 60 m and 200 m horizontal resolution and 0.1 m^2s^{-1} coefficient of horizontal diffusion. The main conclusion from these experiments was that the characteristics of generated short-scale waves are nearly the same in all conducted experiments. This result on the consistency of all model outputs can be explained in terms of the concept of effective horizontal diffusion induced by generated internal waves. In some cases the effective diffusion can be much higher than the background and numerical diffusions. Based on the theory developed by *Young et al.* [1982], shear currents can increase the horizontal diffusion due to vertical diapycnal mixing. The formulae for the calculation of the coefficient of the

effective horizontal diffusion coefficient K_e reads

$$K_e = K_h + \frac{1}{2\omega^2}\left(\frac{du}{dz}\right)^2 \kappa. \quad \text{(B1)}$$

Here du/dz is the velocity shear; ω is the frequency of the oscillating tidal current; K_h and κ are the coefficients of the background horizontal and vertical diffusivity, respectively (for the details of this theory we refer the reader to the original paper). The coefficient of vertical diffusivity κ is set in the model by the *Pacanowski and Philander* [1981] parametrisation (2). The mean value of this coefficient for the whole area over the ADS summit was calculated by time and space averaging of all instant κ profiles over one tidal period. As it was found, the vertical mixing was maximal in the surface 50 m layer; the coefficient κ here was close to the maximal value set in the parametrisation (2). Below this depth κ drops to 0.005 m^2s^{-1} in the layer between 50 and 100 m depth, and to 10^{-3} m^2s^{-1} between 100 and 300 m depth. Having the model output for the horizontal velocity shear, the contribution of the second term in (B1) to K_e was calculated. It was found that K_e was 3 times larger than K_h in the layer 100-200 m depth, and 15 larger than K_h in the subsurface 50-100 m layer. This overwhelming predominance of the wave induced horizontal diffusion over the background and numerical diffusions is the reason why the model was not sensitive to the choice of K_h and the grid resolution.

Acknowledgments. This work was supported by the UK NERC grant NE/K011855/1. The authors would like to thank the captain, the crew and the ROV ISIS team working during the JC136 cruise. The used data are available at https://figshare.com/articles/Untitled_Item/5472451. More details on the 136-th Cruise of the RRS "James Cook" can be found at https://deeplinksproject.wordpress.com/ and https://www.bodc.ac.uk/resources/inventories/cruise_inventory/report/16050/. We

592 are very grateful to the Chief Editor, Associate Editor and two Reviewers for their sup-
593 portive comments, which helped us to focus the manuscript.

References

594 Abarbanel, H.D., D.D. Holm, J.E. Marsden, and T. Ratiu (1984), Richardson number
595 criterion for the nonlinearity of 3D stratified flow. *Phys. Rev. Lett.*, 52, 2352-2355.

596 Aleinik, D.D., G.I. Shapiro, L.D. Mee, and E.M. Lemeshko (2007), Using a lowered acous-
597 tic doppler current profiler for measuring current velocities in the Black Sea. *Oceanology*,
598 *47(1)*, 127-137.

599 Baines, P.G. (1982), On internal tide generation models. *Deep Sea Res. I*, *29 (3A)*, 307–
600 339.

601 Baines, P.G. (2007), Internal tide generation by seamounts. *Deep Sea Res.I*, *54(9)*, 1486–
602 1508, doi:10.1016/dsr.2007.05.009.

603 Egbert, G.D., and S.Y. Erofeeva (2002), Efficient inverse modeling of barotropic ocean
604 tides, *J. Atmos. Oceanic Technol., 19(2)*, 183–204.

605 Flexas, M. M., M. P. Schodlok1, L. Padman, D Menemenlis1, and A. H. Orsi (2015),
606 Role of tides on the formation of the Antarctic Slope Front at the Weddell-Scotia Con-
607 fluence,*J. Geophys. Res.*, 120, 36583680, doi:10.1002/2014JC010372.

608 Gerkema, T. (2001), Internal and interfacial tides: beam scattering and local generation
609 of solitary waves. *J. Mar. Res.*m *59*, 227-255.

610 Haidvogel, D.B., A. Beckmann, D.C. Chapman, and R.-Q. Lin (1993), Numerical simu-
611 lation of flow around a tall isolated seamount. Part II: Resonant Generation of trapped
612 waves. *J. Phys. Oceanogr.*, 23, 2373–2391.

Henry, L.-A., J. Vad, H. S. Findlay, J. Murillo, R. Miligan, and J. M. Roberts (2014), Environmental variability and biodiversity of megabentos on the Hebrides Terrace Seamount (Northeast Atlantic), *Sci. Rep.*, *4*, 5589, doi:10.1038/srep05589(2014).

Howard, L.N. (1961), A note on the paper of John W. Miles. *J. Fluid Mech.*, 10, 509-512.

Huthnance, J.M.(1973), Tidal current asymmetries over the Norfolk sandbanks. *Estuar. Coastal Mar. Sci.*, *1*, 89-99.

Larsson, A.J., J. Järnegren, S.M. Strömberg, M.P. Dahl, T. Lundälv, and S. Brooke (2014) Embryogenesis and larval biology of cold-water coral *Lophelia pertusa*, *PLoS ONE*, 9(7), e102222, doi:101371/journal.pone.0102222.

Lavelle, J.W., and C. Mohn (2010), Motion, commotion, and biophysical connections at deep ocean seamounts. *Oceanography*, 23(1), 91–103.

Loder, J.W. (1980), Topographic rectification of tidal currents on the sides of Georges Bank. *J. Phys. Oceanogr.*, *10*, 1399-1416.

Marshall, J., A. Adcroft, C. Hill, L. Perelman, and C. Heisey (1997), A finite-volume, incompressible Navier-Stokes model for studies of the ocean on the parallel computers, *J. Geophys. Res.*, 102, 5733–5752.

Miles, J.W. (1961), On stability of heterogeneous shear flows. *J. Fluid Mech.*, *10*, 496-508.

Morato, T., S. D. Hoyle, V. Allain, and S. J. Nical (2010), Seamounts are hotspots of pelagic biodiversity in the open ocean, *PNAS*, *107(21)*, 9707–9711, doi:10.1073/pnas.0910290107.

Rogers, A. (1994), The biology of Seamounts, *Advances in Marine Biology, 30*, 305–351.

Pacanowski, R.C., and S. G. H. Philander (1981), Parametrisation of vertical mixing in numerical models of Tropical Oceans, *J. Phys. Oceanogr.*, *11*, 1443-1451.

Pingree, R.D., and L. Maddock (1980), Tidally induced residual flows around an island due to both frictional and rotational effects, *J. Geophys. J. R. Astr. Soc., 63*, 533–546.

Pingree, R.D., and G.T. Mardell (1981), Slope turbulence, internal waves and phytoplankton growth at the Celtic Sea shelf-break, *Phil. Trans. R. Soc. Lond. A*, *302*, 663-682.

Pingree, R.D., and G.T. Mardell (1985) Solitary internal waves in the Celtic Sea. *Prog. Oceanogr.*, *14*, 431-441.

Sherwin, T.J., D. Aleynik, E. Dumont, and M.E. Inall (2015), Deep drivers of mesoscale circulation in the central Rockall Trough. *Ocean Sci.*, *11*, 349–359.

Stashchuk, N., and K. Hutter (2001), Modelling of water exchange through the Strait of the Dardanelles. *Cont. Shelf. Res.*, 21, 1361-1382.

Stashchuk, N., Vlasenko, V., P. Hosegood, and A. Nimmo-Smith (2017), Tidally induced residual current over the Malin Sea continental slope. *Cont. Shelf. Res.*, 139, 21-34.

Stashchuk, N., Vlasenko, V., M.E. Inall, and D. Aleyinik (2014), Horizontal dispersion in shelf seas: High resolution modelling as an aid to sparse sampling. *Progr. Oceanogr.*, 128, 74-87.

Visbeck, M. (2002), Deep velocity profiling using lowered acoustic Doppler current profilers: bottom track and inverse solutions. *J. Atmos. and Ocean Tech.*, *19*,794–807.

Vlasenko, V. (1994), Multimodal soliton of internal waves. *Izvestiya Atmospheric and Oceanic Physics* , *30(2)*, 161–169.

Vlasenko, V., and N. Stashchuk (2006), Amplification and suppression of internal waves by tides over variable bottom topography. *J. of Phys. Oceanogr,*, *36(10)*, 1959–1973.

Vlasenko, V., and N. Stashchuk (2015), Internal tides near the Celtic Sea shelf break: A new look at a well known problem. *Deep Sea Res.I*, *103*, 24–36,

659 doi:10.1016/dsr.2015.05.003.

660 Vlasenko, V., N. Stashchuk, M.R. Palmer, and M.E. Inall (2013), Generation of baroclinic
661 tides over an isolated underwater bank. *J. Geophys. Res.*, 118(9), 4395-4408.

662 Vlasenko V., N. Stashchuk, and K. Hutter (2005), Baroclinic tides: theoretical modeling
663 and observational evidence. Cambridge University Press. 365 pp.

664 Vlasenko V., N. Stashchuk, M. E. Inall, and J. Hopkins (2014), Tidal energy conversion in
665 a global hot spot: on the 3D dynamics of baroclinic tides at the Celtic Sea shelf break,
666 *J. Geophys. Res.*, *119(6)*, 3249–3265, doi:10.1002/2013JC009708.

667 Vlasenko V., N. Stashchuk, M. E. Inall, M. Porter, and D. Aleynik (2016), Fo-
668 cusing of baroclinic tidal energy in a canyon. *J. Geophys. Res. Oceans*, *121*,
669 doi:10.1002/2015JC011314.

670 Wessel, P., D.T. Sandwell, and S.-S. Kim (2010), The global seamount census. *Oceanog-*
671 *raphy*, *23(1)*, 24–33.

672 Young, W.R., P.B. Rhines, and C.J.R. Garrett (1982), Shear-flow dispersion, internal
673 waves and horizontal mixing in the ocean. *J. of Phys. Oceanogr.*, *12*, 515-527.

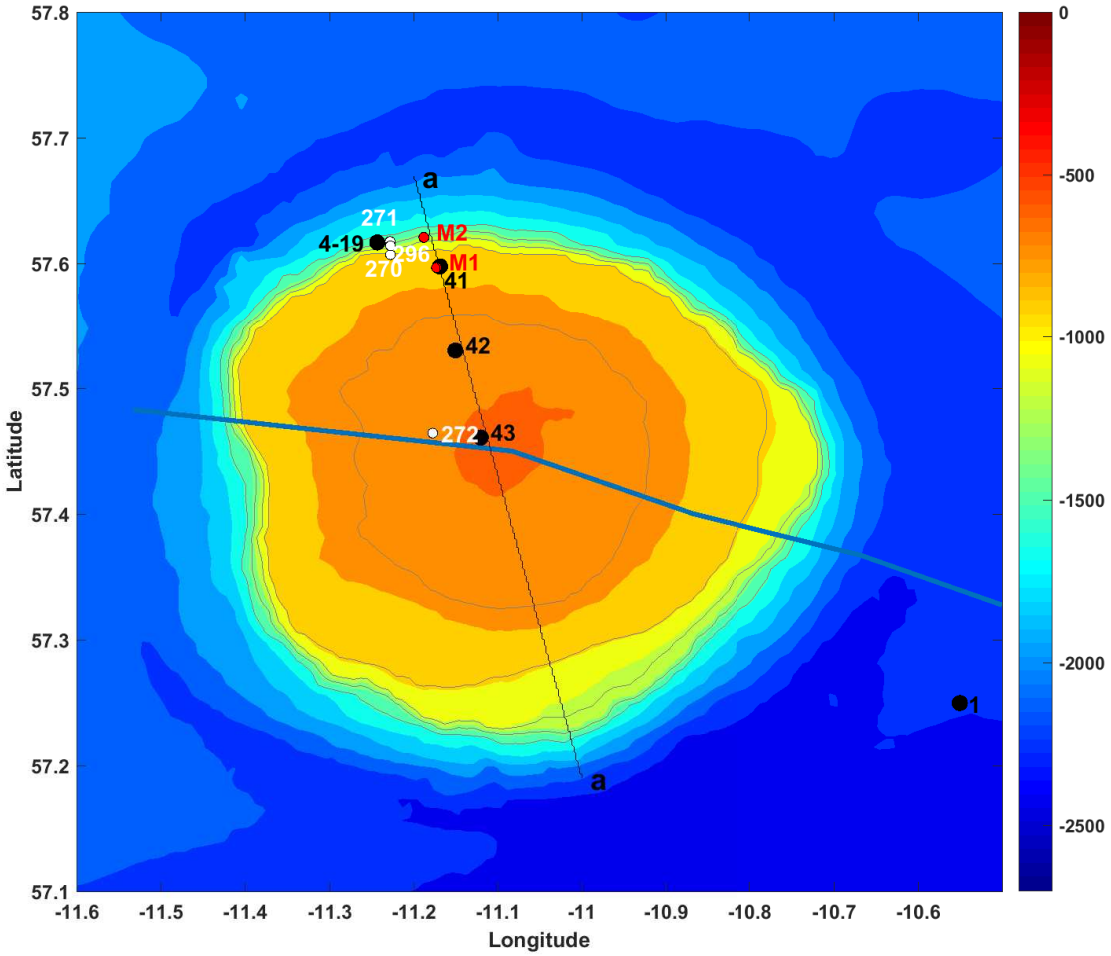

Figure 1. Topography of ADS with positions of CTD stations (black), moorings (red), and ROV dives (white dots). The Ellett Line along which regular CTD surveys have been conducted since 1975 is shown by the blue line (www.o-snap.org). The thin solid line (a-a) shows the transect used for the analysis of the model output.

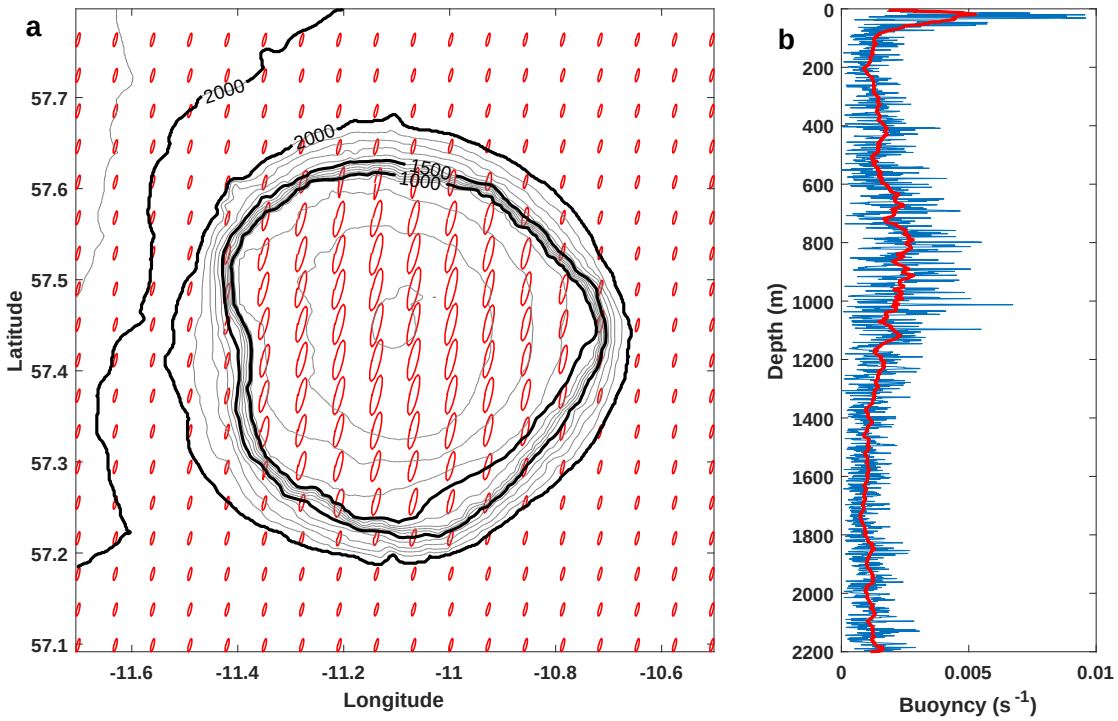

Figure 2. a) Tidal elipses in the area of ADS predicted by the TPXO8.1 inverse tidal model. b) Instant (blue) and smoothed (red) buoyancy frequency profiles recorded at CTD station 1.

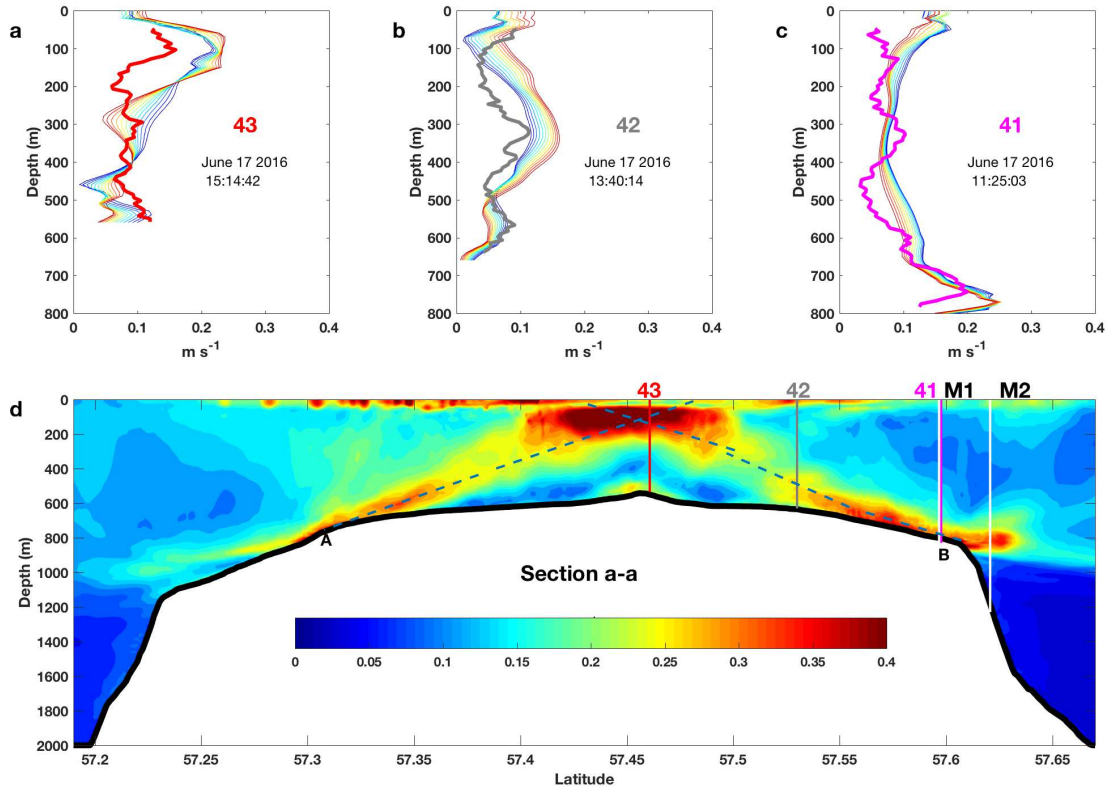

Figure 3. (a-c) Profiles of the horizontal velocity amplitude $\sqrt{u^2+v^2}$ at CTD stations 41-43. Thick lines represent the in-situ recorded profiles, thin coloured lines depict the model predicted curves with five minutes temporal interval starting from the time of real CTD sampling. (d) Model predicted amplitudes of horizontal velocities in the cross-section a-a, Figure 1. Positions of the CTD stations 41-43 and moorings M1 and M2 are shown by vertical lines. Dashed curves depict the positions of tidal beams.

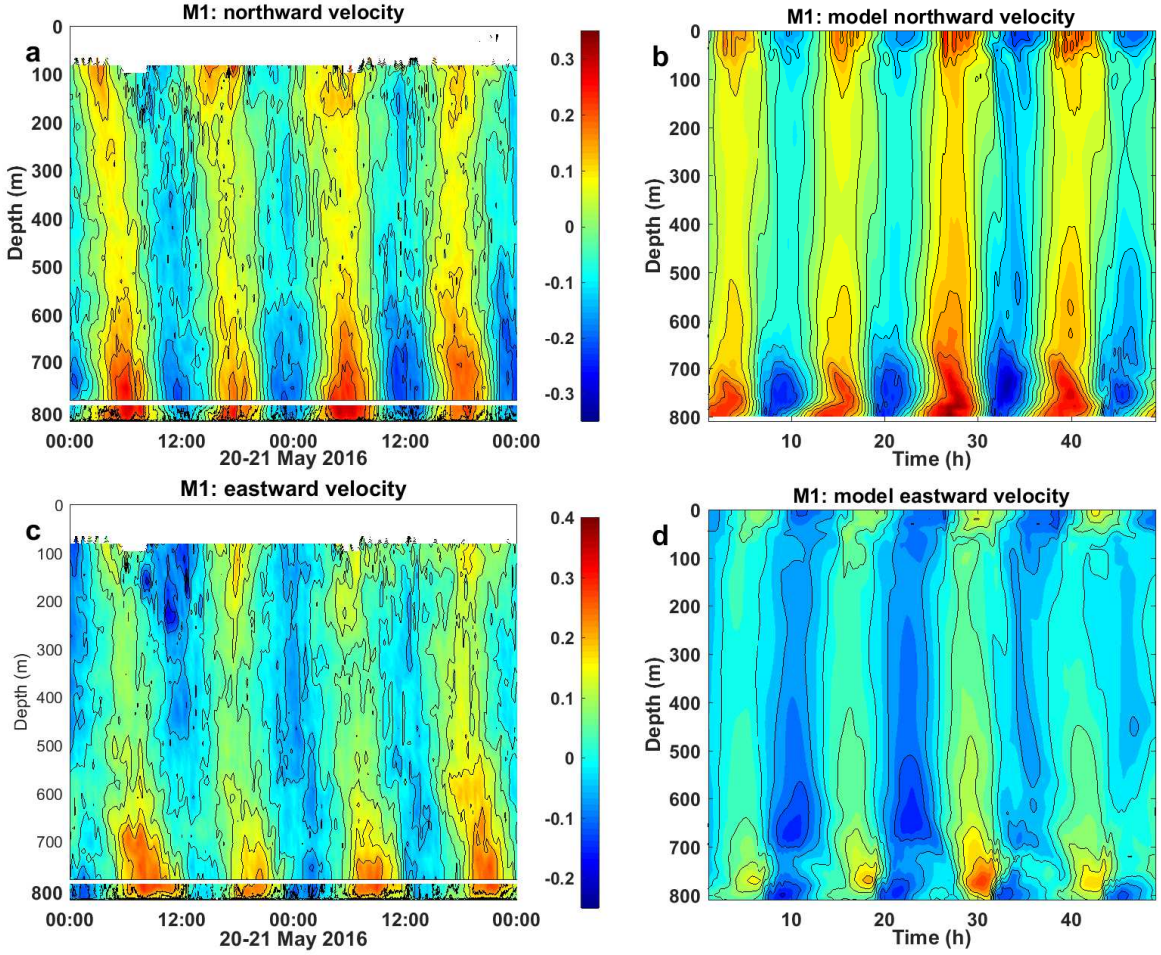

Figure 4. Two day time series of zonal (a,c) and meridional (b,d) velocities recorded at mooring M1 (left column) and predicted by the model (right column).

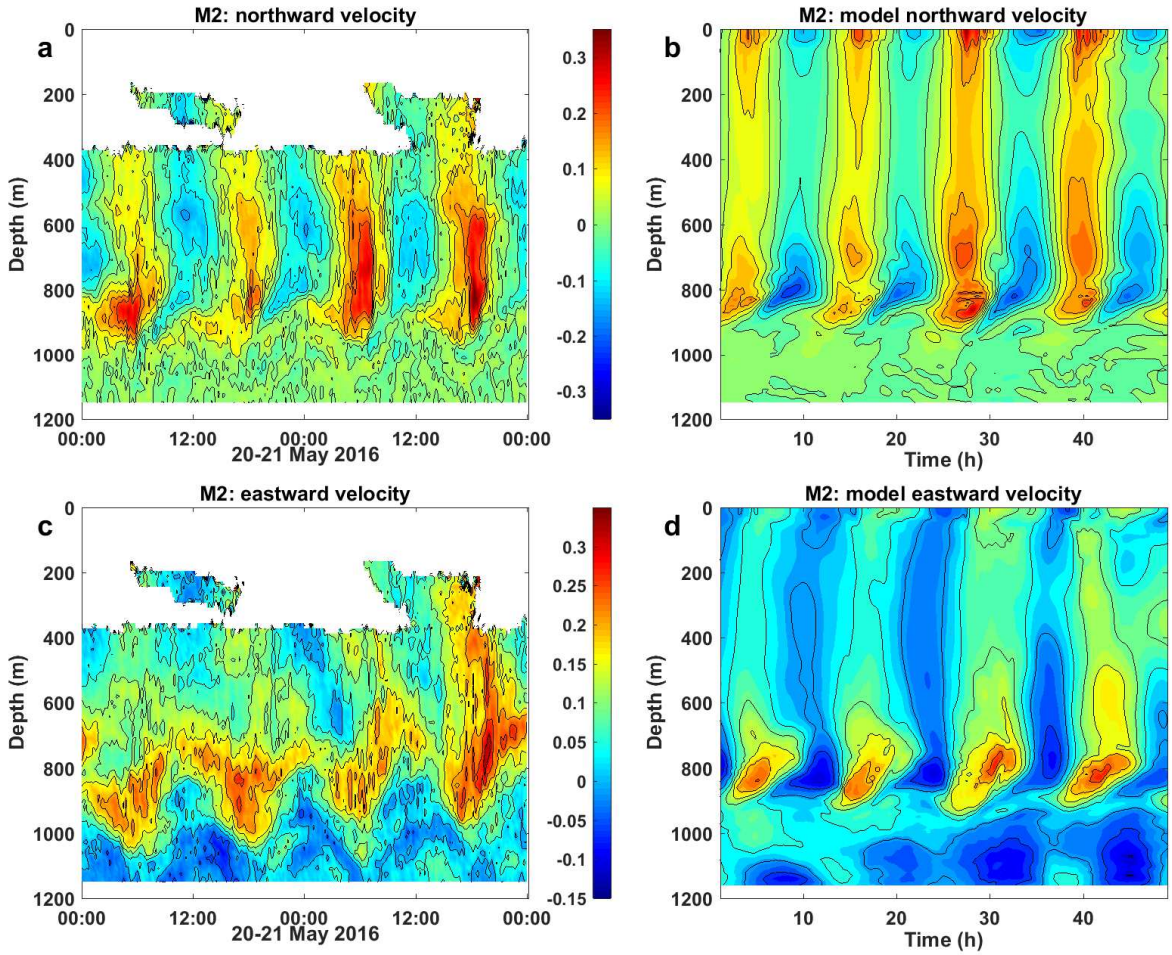

Figure 5. The same as in Figure 4 but for mooring M2.

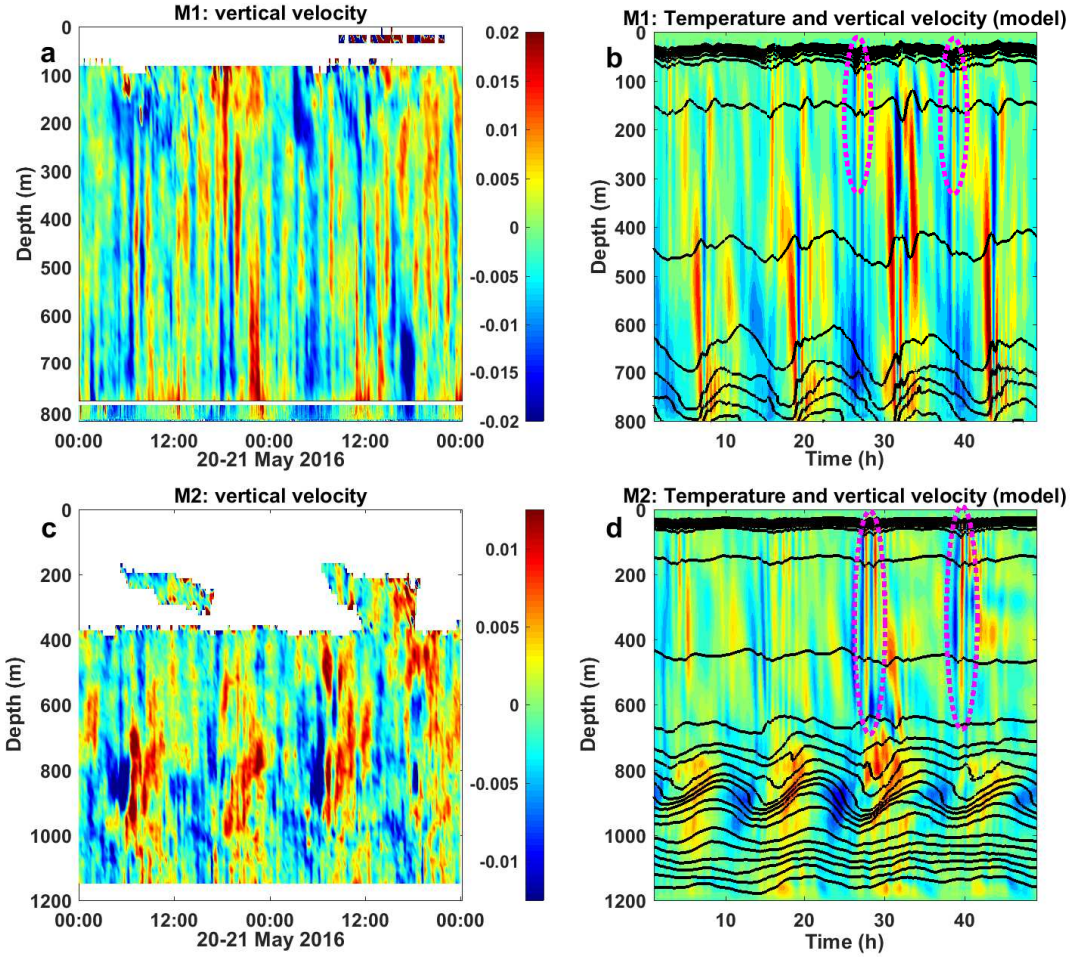

Figure 6. Vertical velocities recorded at moorings M1 and M2 (left) and reproduced by the model (right). The model predicted velocities are overlaid with the temperature field. Red dotted ellipses in panels b and d show the packets of short-scale internal waves.

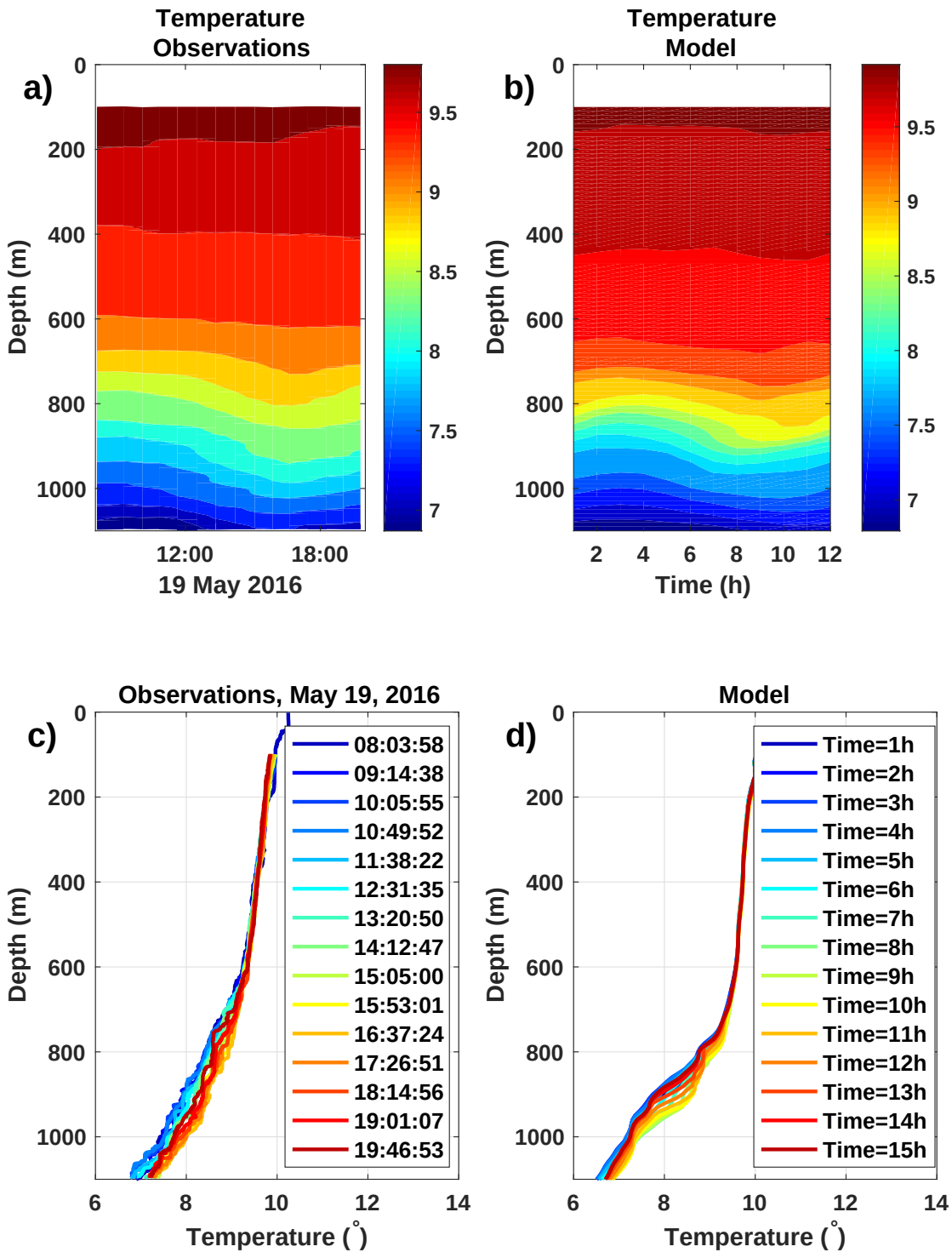

Figure 7. Observational (a) and model predicted (b) temperature time series recorded at the yo-yo CTD station on 19th May 2016. Temperature profiles for the yo-yo station position recorded in-situ (c) and predicted by the model (d).

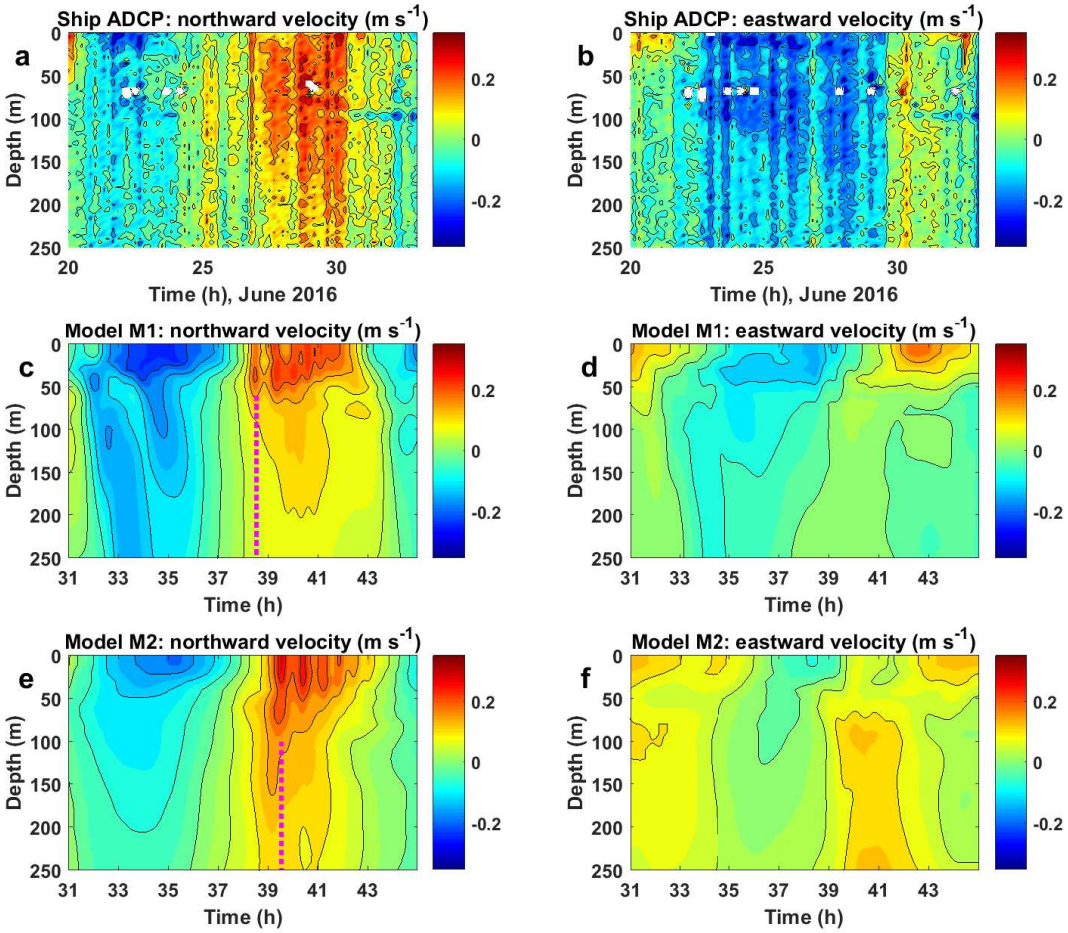

Figure 8. Meridional (left column) and zonal (right column) velocities recorded by the ship mounted ADCP during ROV dive 296 (panels a and b) and predicted by the model (panels c, d, e, and f) at the positions of M1 and M2 moorings during the ROV dive.

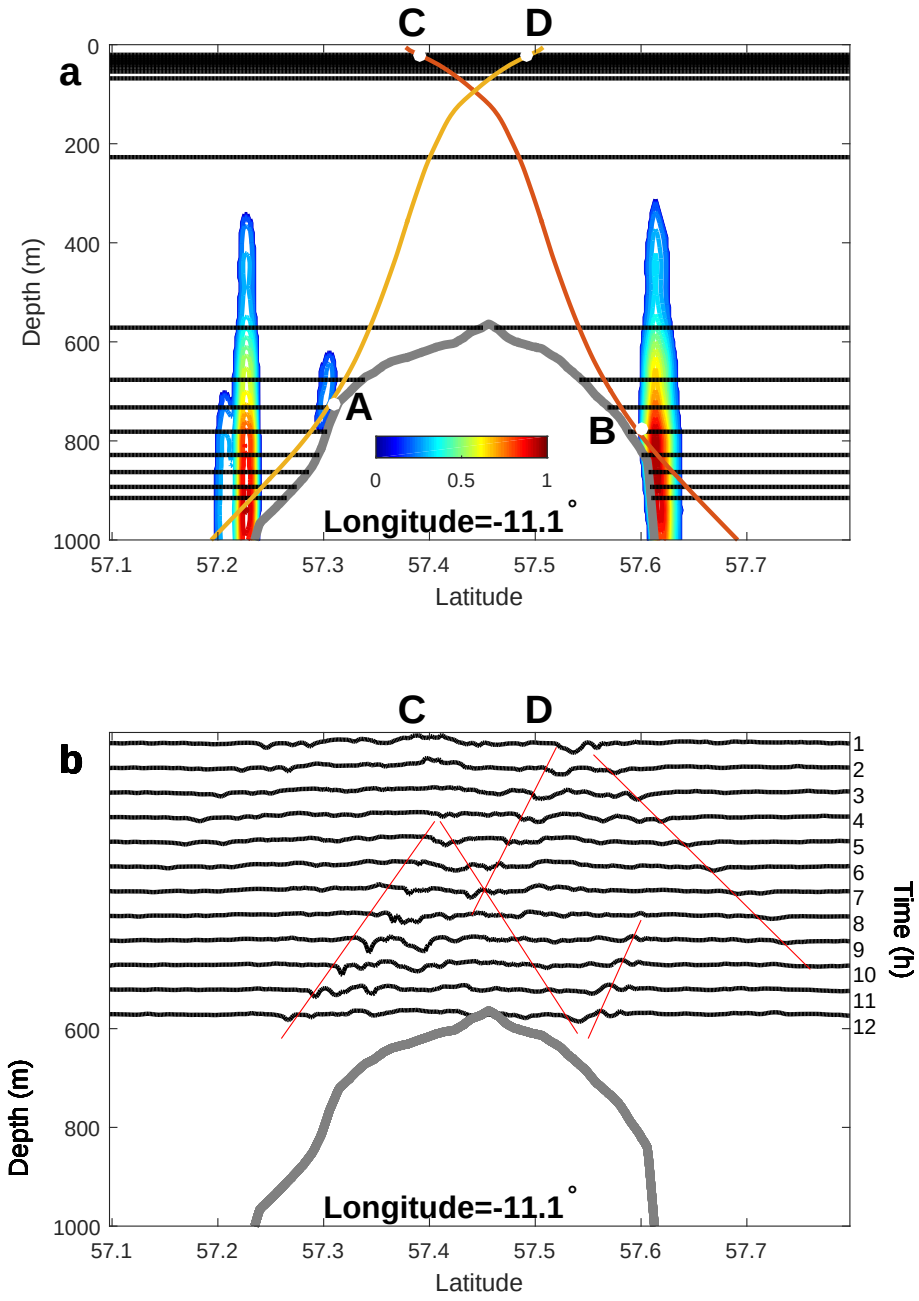

Figure 9. a) Meridional 11.1°W cross-section of undisturbed temperature field through the ADC summit. The interval between isotherms equals 0.25 ^{o}C. Contours AD and BC are characteristic lines (3). Vertically oriented coloured zones show positions of the maxima of normalized IBF (5). b) Hovmöller diagram showing evolution of isotherm 12° along the longitude 11.1°W. Time interval between contours equals 1 hour. The red lines depict the positions of wave packets.

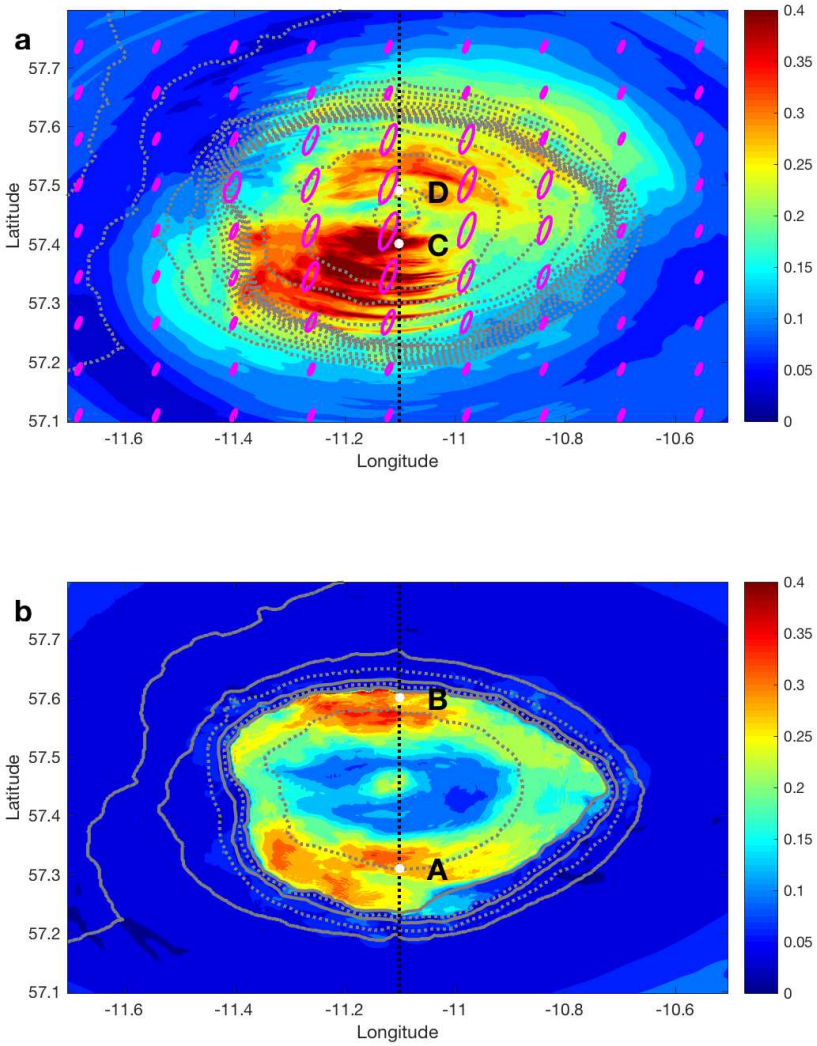

Figure 10. Amplitude of horizontal velocity $\sqrt{u^2+v^2}$ (ms^{-1}) at the free surface (a) and 10 m above the bottom (b). Position of the 11.1°W section is shown by the dashed line. Points A, B, C and D correspond to those shown in Fig. 9.

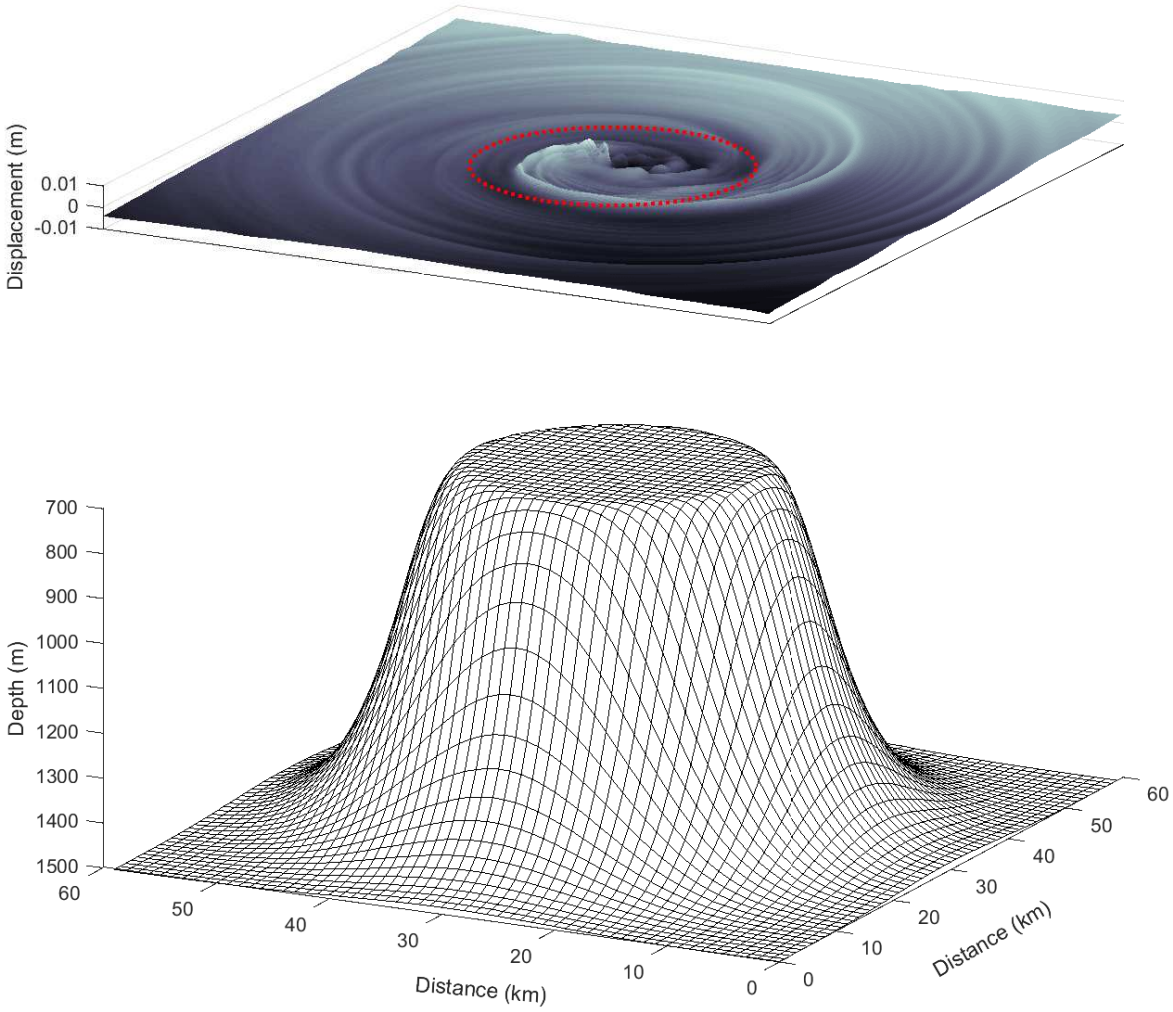

Figure 11. Sea surface displacements produced by internal waves over an isolated symmetrical table seamount. Surface elevations and depressions are shown by white and black colors, respectively. Red dotted line represents a central (flat) part of the bank depicted in the bottom panel.

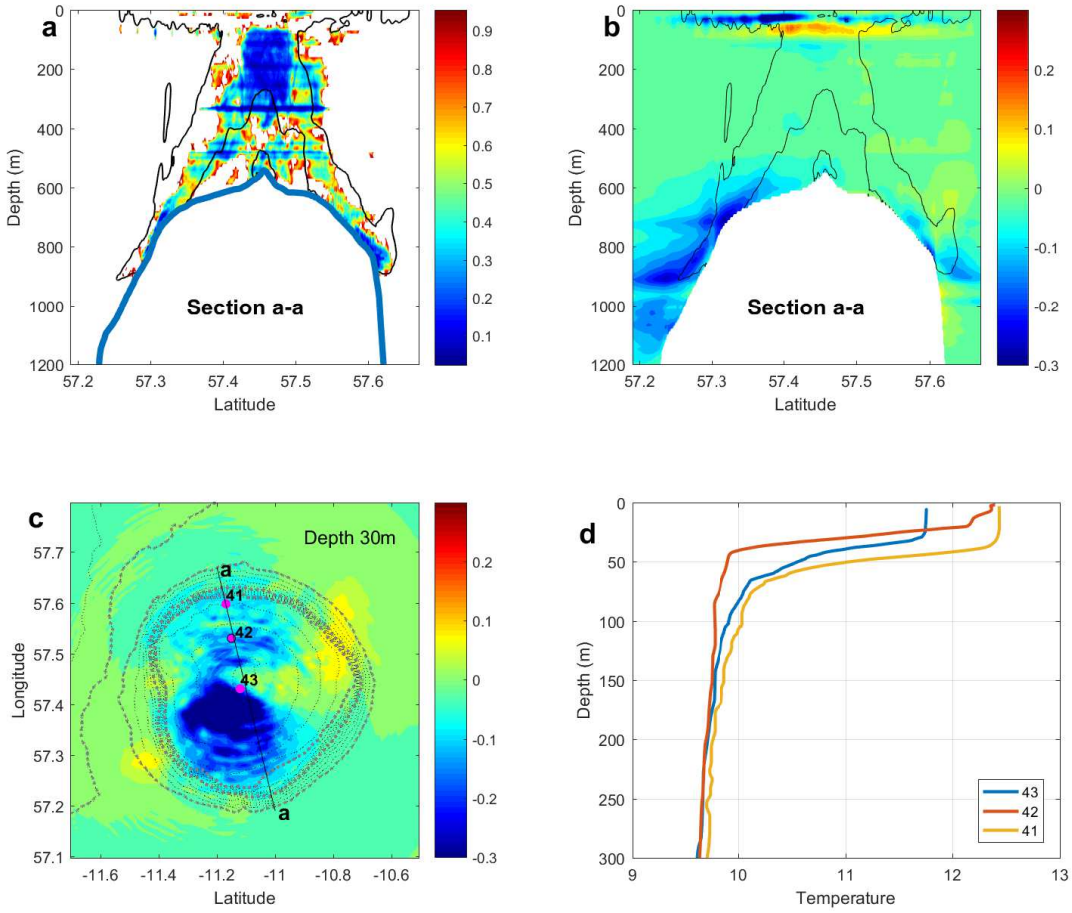

Figure 12. a) Model predicted minimum value of the Richardson number over a tidal period at the transect a-a shown in panels c). b) Difference between initial temperature and that modified by internal wave mixing. The solid black lines in panel a) and b) show velocity magnitude 0.2 $\mathrm{m\,s^{-1}}$. c) Temperature field modifications induced by internal waves in the surface layer. d) Vertical temperature profile recorded at CTD stations 41-43.

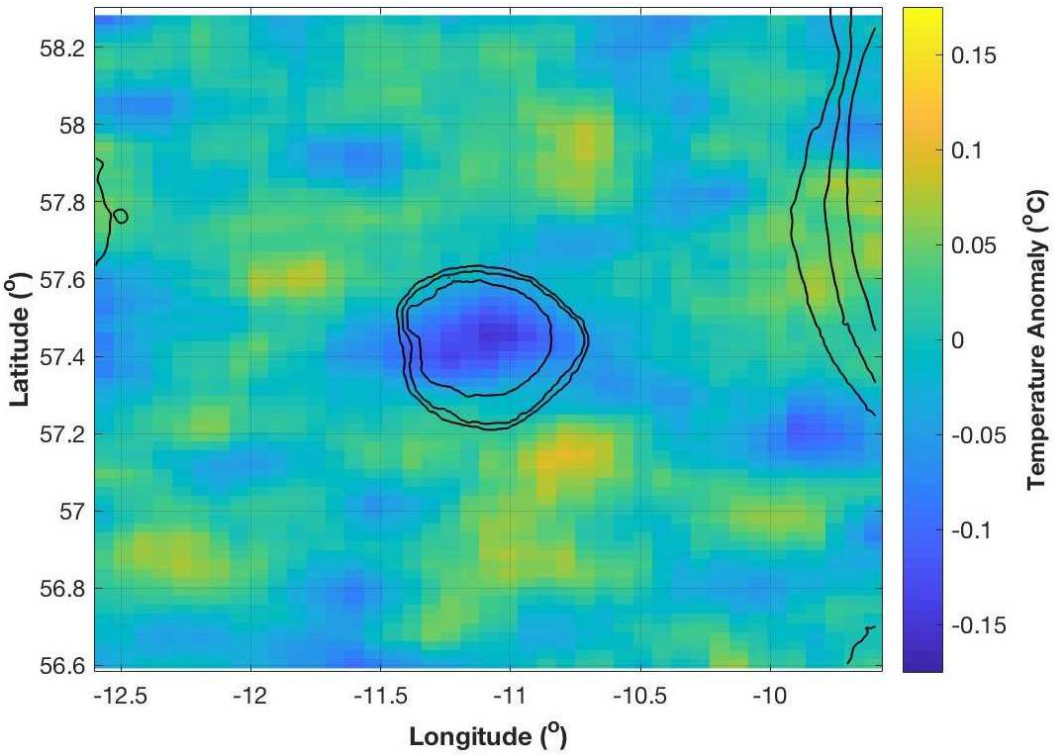

Figure 13. Deviation of the sea surface temperature (SST) from an average SST recorded by MODIS-Aqua satellite in May - August 2003-2016. Large-scale zonal and meridional gradients have been subtracted using a two-dimensional third-order polynomial.

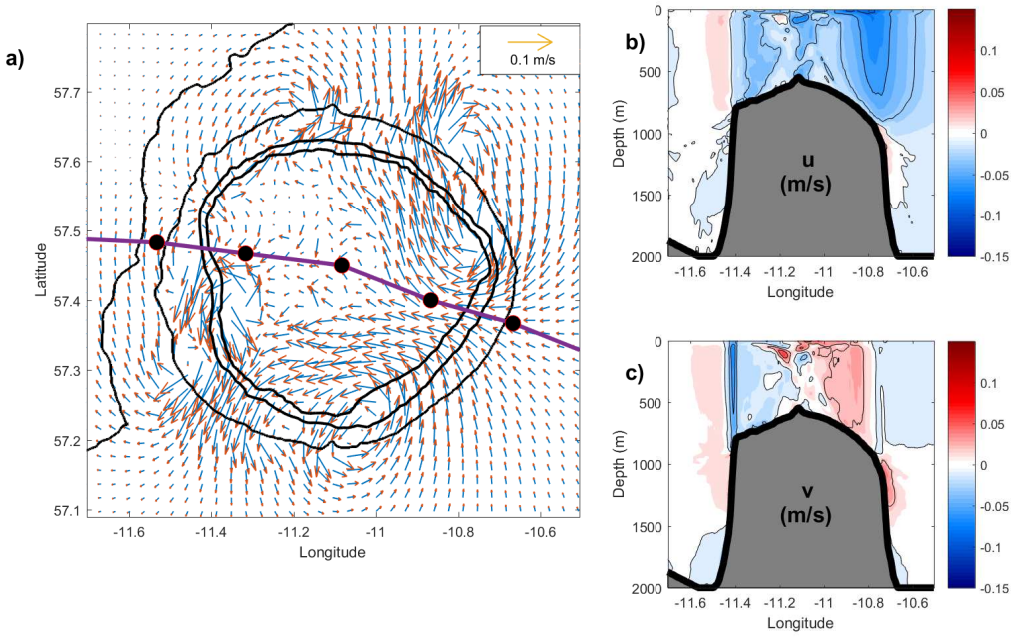

Figure 14. a) Model predicted residual currents generated over ADS at 500-m depth. The velocity fields were averaged over five tidal cycles. The black line with dots shows the Ellet Line. Residual zonal (b) and meridional (c) velocities along the Ellet Line predicted by the model.

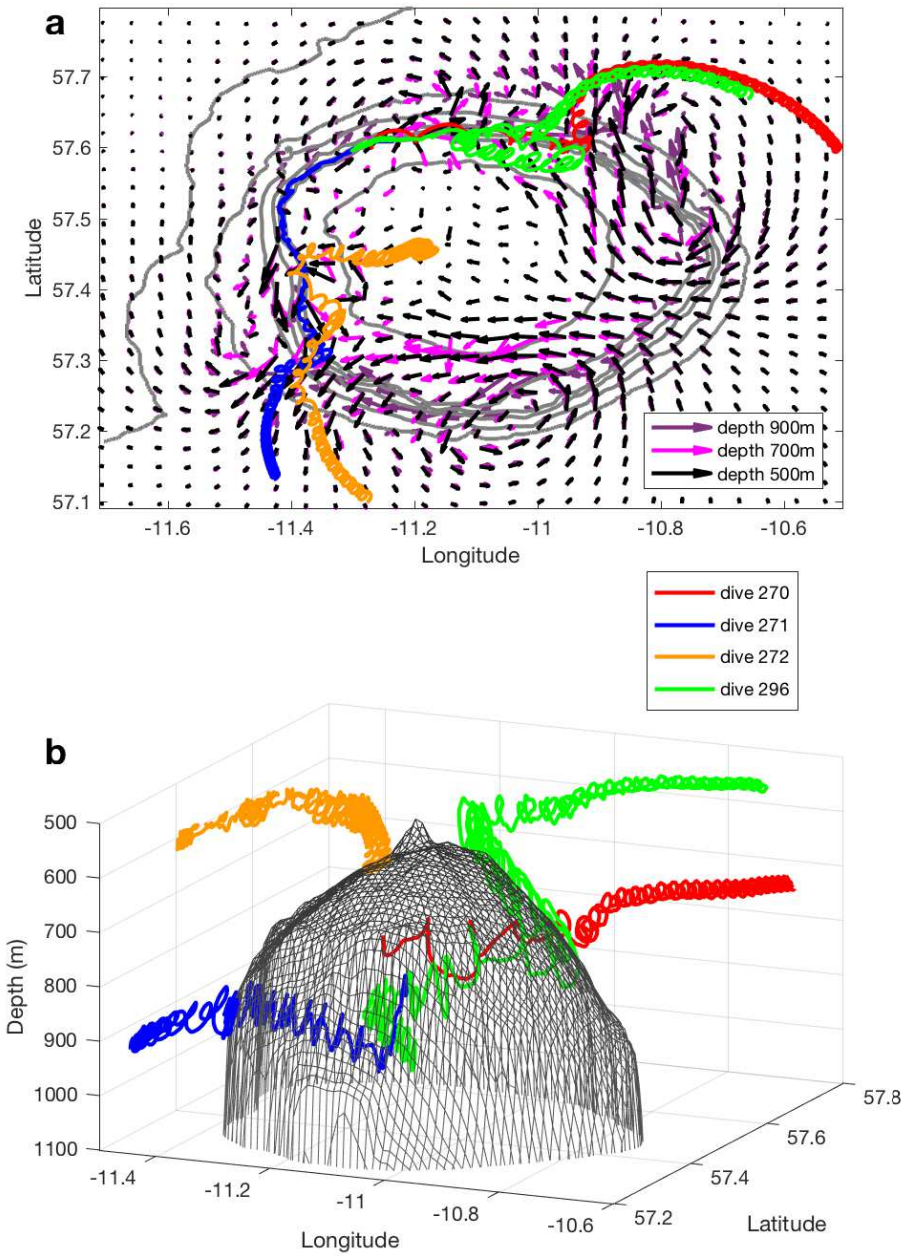

Figure 15. a) Plan view of the trajectories of the particles overlapped with the field of residual currents. b) Three dimensional projection of the particle trajectories.

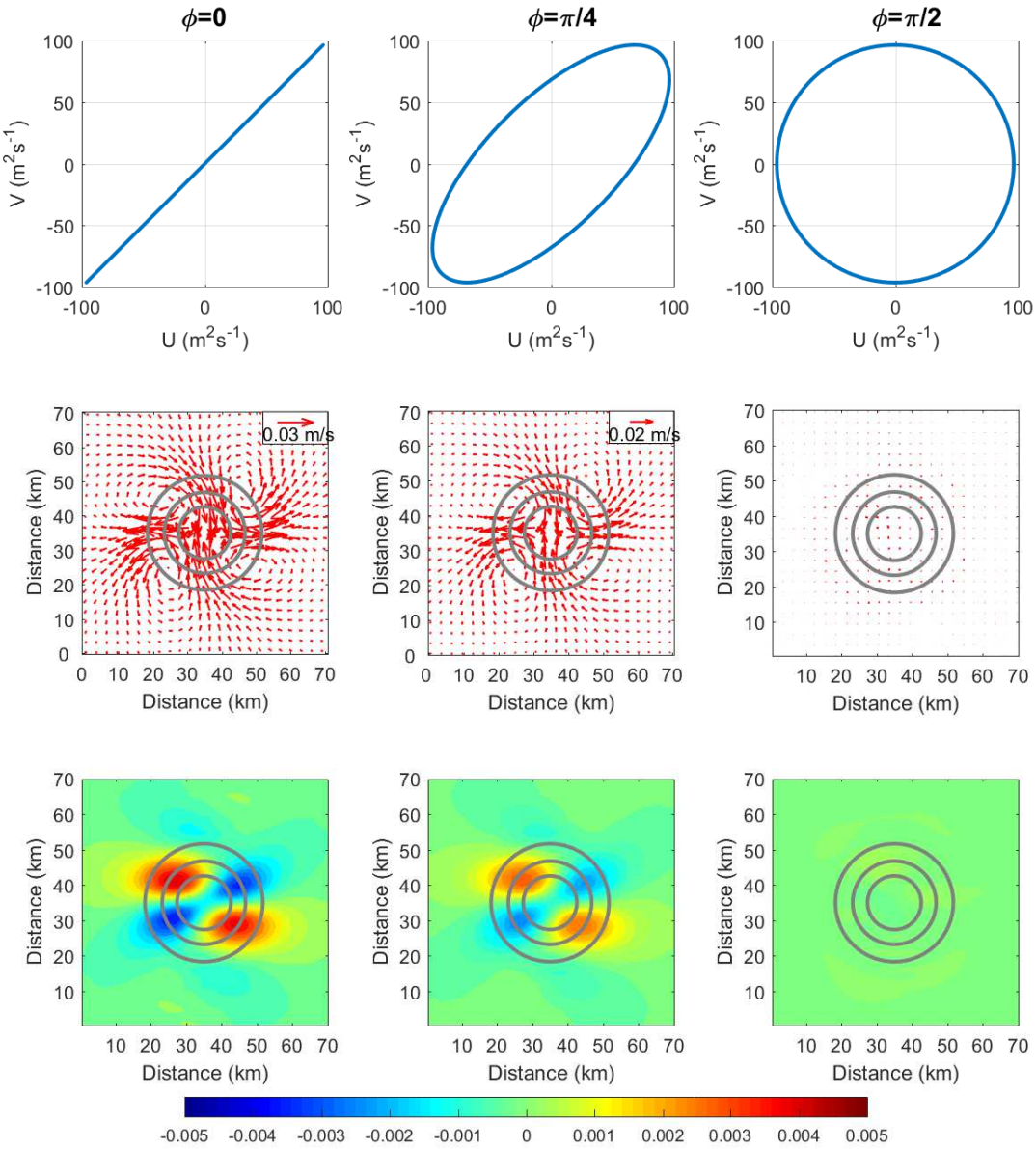

Figure A.1. Residual currents generated by tide over the Gaussian bank (A1) for $A = B = 100\mathrm{m}^2\mathrm{s}^{-1}$ and $\phi = 0$ (left column), $\phi = \pi/4$ (middle column), and $\phi = \pi/2$ (right column). Top row shows the tidal ellipses expressed in terms of water discharge. Middle panels represent the spatial distributions of residual currents. Bottom panels depict the vorticity $u_y - v_x$ (s^{-1}).

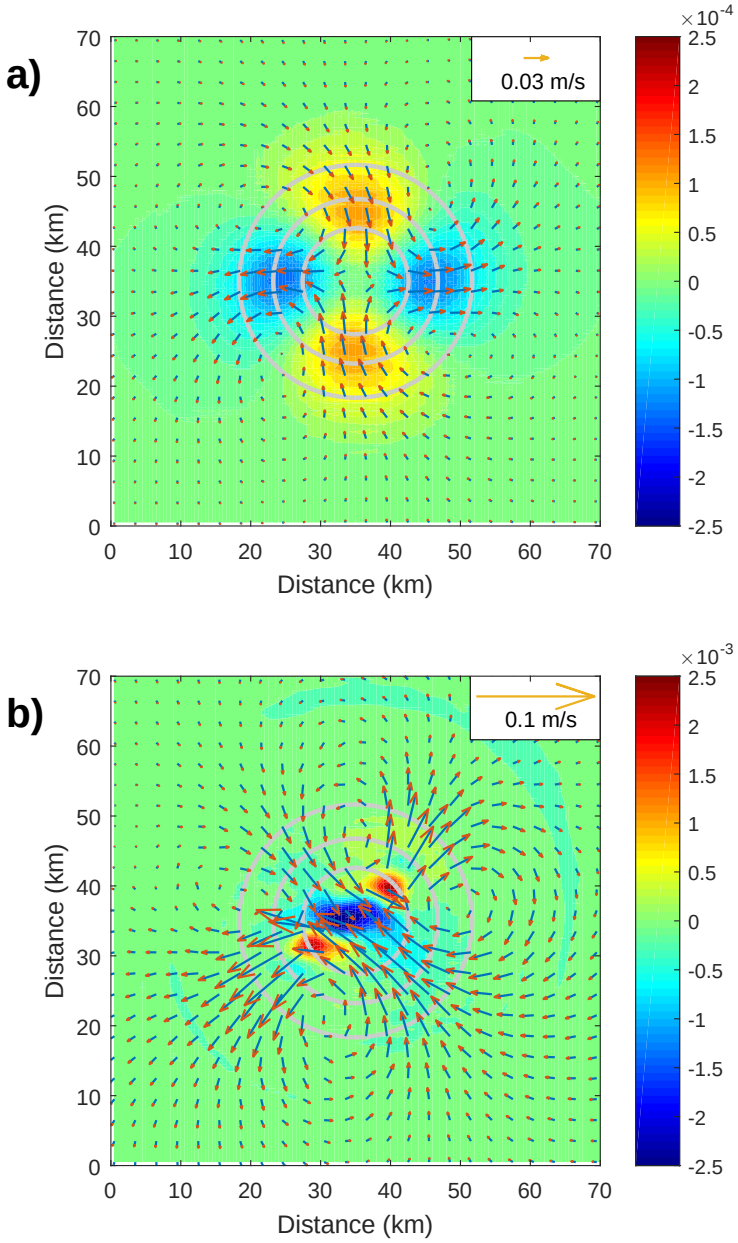

Figure A.2. Spatial distribution of residual currents shown by arrows overlaid with the vertical velocity at the depth of 600 m obtained for homogeneous (a) and stratified (b) fluids.

Table 1. Moorings

Mooring	Longitude	Latitude	Water depth (m)	Frequency (kHz)
M1 (up)	11°10.352′W	57°35.803′N	770	75
M1 (dn)	11°10.352′W	57°35.803′N	780	600
M2 (up)	11°11.250′W	57°37.242′N	1160	75
M2 (dn)	11°11.250′W	57°37.242′N	1170	600

Table 2. Positions of the ROV dives

Dive	Longitude	Latitude	Water depth (m)
270	11°16.062′W	57°35.838′N	826.8
271	11°14.388′W	57°36.504′N	928.3
272	11°10.980′W	57°26.98′N	645.2
296	11°13.590′W	57°36.66′N	1065.2